

## Quarterly Technical Report

## Solid State Research

2001:2

---

### **Lincoln Laboratory**

MASSACHUSETTS INSTITUTE OF TECHNOLOGY

*LEXINGTON, MASSACHUSETTS*



---

Prepared for the Department of the Air Force under Contract F19628-00-C-0002.

Approved for public release; distribution is unlimited.

20011207 095


This report is based on studies performed at Lincoln Laboratory, a center for research operated by Massachusetts Institute of Technology. The work was sponsored by the Department of the Air Force under Contract F19628-00-C-0002.

This report may be reproduced to satisfy needs of U.S. Government agencies.

The ESC Public Affairs Office has reviewed this report, and it is releasable to the National Technical Information Service, where it will be available to the general public, including foreign nationals.

This technical report has been reviewed and is approved for publication.

FOR THE COMMANDER

  
Gary T. Tungian  
Administrative Contracting Officer  
Plans and Programs Directorate  
Contracted Support Management

Non-Lincoln Recipients

PLEASE DO NOT RETURN

Permission is given to destroy this document  
when it is no longer needed.

Massachusetts Institute of Technology  
Lincoln Laboratory

**Solid State Research**

**Quarterly Technical Report**

1 February — 30 April 2001

Issued 30 November 2001

Approved for public release; distribution is unlimited.

## **ABSTRACT**

This report covers in detail the research work of the Solid State Division at Lincoln Laboratory for the period 1 February through 30 April 2001. The topics covered are Quantum Electronics, Electro-optical Materials and Devices, Submicrometer Technology, Biosensor and Molecular Technologies, Advanced Imaging Technology, Analog Device Technology, and Advanced Silicon Technology. Funding is provided by several DoD organizations—including the Air Force, Army, BMDO, DARPA, Navy, NSA, and OSD—and also by the DOE, NASA, and NIST.

## TABLE OF CONTENTS

Abstract	iii
List of Illustrations	vii
List of Tables	xi
Introduction	xiii
Reports on Solid State Research	xv
Organization	xxiii
1. QUANTUM ELECTRONICS	1
1.1 Periodically Poled BaMgF <sub>4</sub> for UV Frequency Generation	1
2. ELECTRO-OPTICAL MATERIALS AND DEVICES	5
2.1 Sensitivity-Bandwidth Product for Electro-optic Modulators	5
2.2 Effect of Substrate Orientation on Phase Separation in Epitaxial GaInAsSb	8
3. SUBMICROMETER TECHNOLOGY	17
3.1 Organic Pellicle Membranes for 157-nm Lithography	17
3.2 High-Resolution Fluorocarbon Based Resist for 157-nm Lithography	20
4. BIOSENSOR AND MOLECULAR TECHNOLOGIES	25
4.1 Response of B Cells to Superparamagnetic Particle Simulants	25
5. ADVANCED IMAGING TECHNOLOGY	31
5.1 Back Illumination of Large-Area CCD Imagers Using Molecular Beam Epitaxy	31

6.	ANALOG DEVICE TECHNOLOGY	35
6.1	Correlation Processor Chip for Noise-Correlation Radar	35
7.	ADVANCED SILICON TECHNOLOGY	47
7.1	Total Dose Radiation Effects on Hardened Buried-Oxide FDSOI NMOS	47

## LIST OF ILLUSTRATIONS

Figure No.		Page
1-1	Transmission for two lengths of BaMgF <sub>4</sub> (BMF) and derived absorption coefficient.	2
1-2	Periodically inverted domains in BMF visualized using an environmental scanning electron micrograph.	3
2-1	Lumped-element electro-optic modulator in which the region indicated has a spatially uniform index varied through the application of voltage $V$ .	7
2-2	Guided-optical structures with dispersive propagation paths: (a) chirped grating reflector, (b) Fabry-Perot resonator with grating reflectors, (c) side-coupled resonant ring.	7
2-3	Atomic force microscope images of (a) Ga <sub>0.9</sub> In <sub>0.1</sub> As <sub>0.09</sub> Sb <sub>0.91</sub> on (001) 2° → (-1-11)A, (b) Ga <sub>0.9</sub> In <sub>0.1</sub> As <sub>0.09</sub> Sb <sub>0.91</sub> on (001) 2° → (1-11)B, (c) Ga <sub>0.9</sub> In <sub>0.1</sub> As <sub>0.09</sub> Sb <sub>0.91</sub> on (001) 2° → (101), (d) Ga <sub>0.82</sub> In <sub>0.18</sub> As <sub>0.16</sub> Sb <sub>0.84</sub> on (001) 2° → (-1-11)A, (e) Ga <sub>0.81</sub> In <sub>0.19</sub> As <sub>0.17</sub> Sb <sub>0.83</sub> on (001) 2° → (1-11)B, and (f) Ga <sub>0.84</sub> In <sub>0.16</sub> As <sub>0.14</sub> Sb <sub>0.86</sub> on (001) 2° → (101). Vertical scale is 5 nm/division in all cases.	10
2-4	High-resolution x-ray diffraction of (a) Ga <sub>0.9</sub> In <sub>0.1</sub> As <sub>0.09</sub> Sb <sub>0.91</sub> on (001) 2° → (1-11)B, (b) Ga <sub>0.82</sub> In <sub>0.18</sub> As <sub>0.16</sub> Sb <sub>0.84</sub> on (001) 2° → (-1-11)A, (c) Ga <sub>0.81</sub> In <sub>0.19</sub> As <sub>0.17</sub> Sb <sub>0.83</sub> on (001) 2° → (1-11)B, and (d) Ga <sub>0.84</sub> In <sub>0.16</sub> As <sub>0.14</sub> Sb <sub>0.86</sub> on (001) 2° → (101).	12
2-5	Photoluminescence spectra measured at 4 and 300 K of (a) Ga <sub>0.9</sub> In <sub>0.1</sub> As <sub>0.09</sub> Sb <sub>0.91</sub> on (001) 2° → (1-11)B, (b) Ga <sub>0.82</sub> In <sub>0.18</sub> As <sub>0.16</sub> Sb <sub>0.84</sub> on (001) 2° → (-1-11)A, (c) Ga <sub>0.81</sub> In <sub>0.19</sub> As <sub>0.17</sub> Sb <sub>0.83</sub> on (001) 2° → (1-11)B, and (d) Ga <sub>0.84</sub> In <sub>0.16</sub> As <sub>0.14</sub> Sb <sub>0.86</sub> on (001) 2° → (101).	13
3-1	(a) Spectral transmission of as-received pellicle material before and after lamp cleaning, and (b) average 157-nm transmission values of the pellicle material as a function of lamp cleaning time.	18

## LIST OF ILLUSTRATIONS (Continued)

Figure No.		Page
3-2	Laser-based testing of two freestanding pellicles under 1 and 100 ppm O <sub>2</sub> , respectively.	19
3-3	(a) Transmission of laser-irradiated freestanding pellicle material immediately after irradiation and after lamp-based cleaning. (b) Comparisons of laser-induced losses prior to and after lamp cleaning.	19
3-4	Fluorocarbon based 157-nm resist (LUVR-20012) at 100-nm thickness patterned with 250–150-nm features using a 0.50-NA Schwartzschild lens.	22
3-5	Fluorocarbon based 157-nm resist (LUVR-20007) at 100-nm thickness patterned with 40-nm dense lines on a 100-nm pitch using an interference lithography system: (a) top-down view of features and (b) cross-sectional view showing standing waves in the resist sidewalls.	23
4-1	Centrifugation enhanced CANARY (Cellular Analysis and Notification of Antigen Risks and Yields) format. Top: Photographs of centrifugation setup in spinning and measuring modes. Bottom: Plot of photon output produced by exposure of 25,000 B cells to 530,000 killed tularemia particles with and without centrifugation enhancement procedures as indicated in the schematic at right, where tularemia particles are represented by black circles and B cells by larger red circles.	26
4-2	Detection of killed tularemia by CANARY B cells: (a) dose response for B cells exposed to the numbers of tularemia particles and control samples indicated, showing the broad dynamic range and extreme specificity of this identification sensor technology, and (b) typical unfiltered data demonstrating excellent signal-to-background ratios for identification of 60 tularemia particles.	28
4-3	Design and dimensions of the portable CANARY microcentrifuge sensor prototype built for live agent testing and other collaborative development work requiring a portable sensor unit.	29
5-1	Quantum efficiency of back-side-illuminated CCD in the visible and near visible.	32



## LIST OF ILLUSTRATIONS (Continued)

Figure No.		Page
6-1	Scenario in which a noise-correlation radar might be used, illustrating some of its unusual characteristics, such as the very high pulse repetition frequency that results in multiple transmitted pulses in space at any given time.	37
6-2	Block diagram of real-time correlation processor chip. The red section operates at the full radar clock frequency of 1 GHz, capturing and storing reference and signal data from the radar at times that it computes based on radar operating parameters written to the chip. The green section processes the data at a lower, "correlator" clock frequency of 280 MHz. The blue section, which can operate at 55 MHz, provides communication with the rest of the signal processing system.	38
6-3	Image of the chip layout. The chip is 5 mm on a side.	42
6-4	Waveforms recorded on an oscilloscope with the chip operating at its full design frequency. The upper trace shows the input RGATE signal that starts the processing of a new coherent processing interval. The middle trace shows the waveform on the RFLD diagnostic output. Each negative pulse shows when reference data about the signal transmitted by the radar are recorded on the chip. The time between pulses is the programmed "pulse repetition interval" for the radar. The bottom trace shows the waveform on the SFLD diagnostic output. Each negative pulse shows when data about the signal received by the radar are stored in one of the two memory banks on the chip. These pulses are delayed from their corresponding RFLD pulses by the programmed target range delay, adjusted for range walk.	43
6-5	Additional waveforms recorded with the chip operating at its full design frequency. The upper trace again shows the input RGATE. The lower two traces show the waveforms on the diagnostic outputs AFLD and BFLD, where negative pulses indicate when correlation data are being stored into each of the two banks of "presum" memory. The chip has been programmed to perform a presum of five pulses.	44

## LIST OF ILLUSTRATIONS (Continued)

Figure No.		Page
6-6	Processed correlation data read from the chip with the radar clock at 800 MHz. The solid curve is the in-phase component PSMCI; the dotted curve is the quadrature component PSMCQ. Both signals have been scaled to take out factors arising from the cosine/sine weighting and the presum value. The signal in-phase input SI was a square wave with 128 0's and 128 1's. The reference in-phase input RI was a section from that square wave comprising 72 0's followed by 40 1's. The quadrature inputs were both 0. The observed output is exactly what theory predicts: linear ramps between baselines at half the code length ( $112/2 = 56$ in this case) and values reduced from that by the number of 0's (for PSMCI) and 1's (for PSMCQ) in the reference pattern.	45
7-1	Schematic diagram describing MIT Lincoln Laboratory's 0.25- $\mu\text{m}$ fully depleted silicon-on-insulator (FDSOI) CMOS process.	48
7-2	Front-channel $I_D V_G$ at $V_D = 50$ mV (wafer bias 0 V) for $W = 4.8$ $\mu\text{m}$ , $L = 0.5$ $\mu\text{m}$ NMOS on (a) control Advantox150 <sup>TM</sup> and (b) radhard Advantox150 <sup>TM</sup> substrates for total X-ray radiation dose up to 1 Mrad ( $\text{SiO}_2$ ).	49
7-3	(a) Front-channel threshold shift $V_{t,low}$ at $V_D = 50$ mV and (b) subthreshold voltage swing vs total radiation dose for $W = 4.8$ $\mu\text{m}$ , $L = 0.5$ $\mu\text{m}$ NMOS fabricated on control and radhard Advantox150 <sup>TM</sup> wafers.	50
7-4	Front-channel $I_D V_G$ at $V_D = 50$ mV with back gate accumulated (wafer bias -30 V) for $W = 4.8$ $\mu\text{m}$ , $L = 0.5$ $\mu\text{m}$ NMOS on radhard Advantox150 <sup>TM</sup> substrates for total X-ray radiation dose up to 1 Mrad ( $\text{SiO}_2$ ).	50
7-5	Back-channel $I_D V_W$ at $V_D = 50$ mV (gate bias 0 V) for $W = 4.8$ $\mu\text{m}$ , $L = 0.5$ $\mu\text{m}$ NMOS on (a) control Advantox150 <sup>TM</sup> and (b) radhard Advantox150 <sup>TM</sup> wafers for total X-ray radiation dose up to 1 Mrad ( $\text{SiO}_2$ ).	51
7-6	Front-channel $I_D V_G$ at $V_D = 2$ V (wafer bias 0 V) for $W = 4.8$ , $L = 0.5$ $\mu\text{m}$ NMOS on (a) control and (b) radhard Advantox150 <sup>TM</sup> substrates for total X-ray radiation dose up to 1 Mrad ( $\text{SiO}_2$ ).	52

## LIST OF ILLUSTRATIONS (Continued)

Figure No.		Page
7-7	(a) Front-channel threshold shift $V_{t,high}$ at $V_D = 2$ V and (b) off-state leakage current $I_D$ at $V_G = 0$ V and $V_D = 2$ V vs total radiation dose for $W = 4.8$ $\mu\text{m}$ , $L = 0.5$ $\mu\text{m}$ NMOS fabricated on control radhard Advantox150™ wafers.	53

## LIST OF TABLES

Table No.		Page
2-1	Photoluminescence Data of GaInAsSb	14
3-1	Comparison of Hydroxystyrene Polymer with Several Hexafluoroisopropanol Styrene Polymers All Containing a 60:40 Copolymer Ratio	21
6-1	List of All Parameters Whose Values Are Loaded into Correlator Chip to Control Its Normal Operation	40

## INTRODUCTION

### 1. QUANTUM ELECTRONICS

Ferroelectric domain inversion and excellent uv optical transparency has been demonstrated in BaMgF<sub>4</sub>. By using quasi-phase-matching techniques, frequency conversion to wavelengths <150 nm should be possible.

### 2. ELECTRO-OPTICAL MATERIALS AND DEVICES

For lumped-element electro-optic modulators the sensitivity  $\partial\phi/\partial V$  of the phase  $\phi$  in response to an applied voltage  $V$  is related to the optical group delay  $T_g$  and bandwidth  $\Delta\omega$ , and this relationship imposes a fundamental tradeoff between the sensitivity and bandwidth of electro-optic modulators:  $(\partial\phi/\partial V)\Delta\omega = (dn/dV)(\omega/n)$ , where  $n$  is the optical index. A similar relationship for traveling-wave modulators sets an upper limit on  $\partial\phi/\partial V$  proportional to  $T_g$ .

The substrate misorientation has been found to have a significant effect on the extent of phase separation in Ga<sub>1-x</sub>In<sub>x</sub>As<sub>y</sub>Sb<sub>1-y</sub> grown nominally lattice matched to GaSb. Phase separation is reduced in layers grown on (001) 2° → (1-11)B substrates compared to those grown on (001) 2° → (-1-11)A and (001) 2° → (101) substrates, and can be attributed to the smaller adatom diffusion length on substrates miscut toward (1-11)B.

### 3. SUBMICROMETER TECHNOLOGY

New fluorocarbon polymers have been synthesized with transparencies approaching 95% at 157 nm for 1-μm-thick films. The durability of these films has been tested for use as protective pellicles for 157-nm-wavelength projection lithography.

A number of unique 4-hexafluoroisopropanol styrene based polymer systems capable of sub-100-nm imaging at a resist thickness of 100 nm or more have been synthesized and tested. Fluorine-functionalized polymers are more transparent in the 157-nm spectral region than the pure hydrocarbon polymers used in conventional deep uv resists.

### 4. BIOSENSOR AND MOLECULAR TECHNOLOGIES

B cells that emit light when exposed to viral and bacterial pathogens have been produced and used to evaluate the performance of the CANARY (Cellular Analysis and Notification of Antigen Risks and Yields) sensor. A centrifugation-assisted CANARY assay has been developed which enables the rapid detection of very small numbers of bacteria.

## **5. ADVANCED IMAGING TECHNOLOGY**

Large-area CCD imagers have been successfully processed through back illumination, using molecular beam epitaxy as the passivation treatment. The technique has yielded devices with nearly 100% internal quantum efficiency from 200 to 1100 nm.

## **6. ANALOG DEVICE TECHNOLOGY**

A processor chip has been developed for an advanced noise-correlation radar. The radar uses true random noise as its modulation source, and because the processing gain possible with random noise signals is limited, coherent processing over a large number of code "chips" is required.

## **7. ADVANCED SILICON TECHNOLOGY**

Silicon-on-insulator (SOI) substrates have been fabricated to enhance the radiation hardness of sub-micron fully depleted SOI NMOS up to at least 1 Mrad ( $\text{SiO}_2$ ). The radiation hardness is shown to be associated with the reduction in threshold voltage shift of the back channel formed by the SOI/buried oxide.

## REPORTS ON SOLID STATE RESEARCH

1 FEBRUARY THROUGH 30 APRIL 2001

### PUBLICATIONS

- |  |  |   |
|--|--|---|
| Temperature Dependence of the Breakdown Voltage for Reverse-Biased GaN p-n-n <sup>+</sup> Diodes | R. L. Aggarwal<br>I. Melngailis<br>S. Verghese<br>R. J. Molnar<br>M. W. Geis<br>L. J. Mahoney                      | <i>Solid State Commun.</i> <b>117</b> , 549 (2001)              |
| Photon Recycling and Recombination Processes in 0.53 eV p-Type InGaAsSb                          | J. M. Borrego*<br>S. Saroop*<br>R. J. Gutmann*<br>G. W. Charache*<br>T. Donovan*<br>P. F. Baldasaro*<br>C. A. Wang | <i>J. Appl. Phys.</i> <b>89</b> , 3753 (2001)                   |
| MEMS Microswitches for Reconfigurable Microwave Circuitry  | S. M. Duffy*<br>C. O. Bozler<br>S. Rabe<br>J. M. Knecht<br>L. Travis<br>P. W. Wyatt<br>C. L. Keast<br>M. A. Gouker | <i>IEEE Microw. Wirel. Compon. Lett.</i> <b>11</b> , 106 (2001) |
| Impurity Band in the Interfacial Region of GaN Films Grown by Hydride Vapor Phase Epitaxy        | J. W. P. Hsu*<br>D. V. Lang*<br>S. Richter*<br>R. N. Kleiman*<br>A. M. Sergent*<br>D. C. Look*<br>R. J. Molnar     | <i>J. Electron. Mater.</i> <b>30</b> , 115 (2001)               |

---

\*Author not at Lincoln Laboratory.

Surface Morphology and  
Electronic Properties of  
Dislocations in AlGaIn/GaN  
Heterostructures

J. W. P. Hsu\*  
M. J. Manfra  
D. V. Lang\*  
K. W. Baldwin\*  
L. N. Pfeiffer\*  
R. J. Molnar

*J. Electron. Mater.* **30**, 110  
(2001)

Inhomogeneous Spatial Distribution  
of Reverse Bias Leakage in GaN  
Schottky Diodes

J. W. P. Hsu\*  
M. J. Manfra  
D. V. Lang\*  
S. Richter\*  
S. N. G. Chu\*  
A. M. Sergent\*  
R. N. Kleiman\*  
L. N. Pfeiffer\*  
R. J. Molnar

*Appl. Phys. Lett.* **78**, 1685  
(2001)

Measurement of Mode-Locked  
Laser Timing Jitter by Use of  
Phase-Encoded Optical Sampling

P. W. Juodawlkis  
J. C. Twichell  
J. L. Wasserman  
G. E. Betts  
R. C. Williamson

*Opt. Lett.* **26**, 289 (2001)

Dislocation-Independent Mobility  
in Lattice-Mismatched Epitaxy:  
Application to GaN

D. C. Look\*  
C. E. Stutz\*  
R. J. Molnar  
K. Saarinen\*  
Z. Liliental-Weber\*

*Solid State Commun.* **117**, 571  
(2001)

Intermodulation Distortion and  
Josephson Vortices in YBCO  
Bicrystal Grain Boundaries

D. E. Oates  
H. Xin\*  
G. Dresselhaus\*  
M. S. Dresselhaus\*

*IEEE Trans. Appl. Supercon.*  
**11**, 2804 (2001)

---

\*Author not at Lincoln Laboratory.

Optoelectronic Device  
Performance on Reduced  
Threading Dislocation Density  
GaAs/Si

P. J. Taylor  
W. A. Jesser\*  
J. D. Benson\*  
M. Martinka\*  
J. H. Dinan\*  
J. Bradshaw\*  
M. Lara-Taysing\*  
R. P. Leavitt\*  
G. Simonis\*  
W. Chang\*  
W. W. Clark III\*  
K. A. Bertness\*

*J. Appl. Phys.* **89**, 4365 (2001)

Effects of Crosstalk in  
Demultiplexers for Photonic  
Analog-to-Digital Converters

R. C. Williamson  
P. W. Juodawlkis  
J. L. Wasserman  
G. E. Betts  
J. C. Twichell

*J. Lightwave Technol.* **19**, 230  
(2001)

#### PRESENTATIONS<sup>†</sup>

Three-Dimensional Integrated  
Circuits for Low-Power High-  
Bandwidth Systems on a Chip

J. A. Burns  
C. L. Keast  
P. W. Wyatt  
K. Warner  
A. Loomis  
L. McGrath\*  
C. Lewis\*

IEEE International Solid-State  
Circuits Conference,  
San Francisco, California,  
5-7 February 2001

Evidence for Impurity Effects and  
Spatial Inhomogeneity on  
Nonlinear Microwave Impedance

D. E. Oates

Office of Naval Research  
Annual Review of  
Superconducting Electronics,  
Sedona, Arizona,  
8-11 February 2001

---

\*Author not at Lincoln Laboratory.

<sup>†</sup> Titles of presentations are listed for information only. No copies are available for distribution.



Passively *Q*-Switched Microchip  
Lasers and Applications

J. J. Zayhowski

Lincoln Laboratory  
Technical Seminar Series,  
Old Dominion University,  
Norfolk, Virginia,  
9 February 2001

Placement of Biological Agent  
Detectors for Optimum  
Performance

T. H. Jeys  
J. R. Ochoa

2001 MASINT Biological  
Warfare Science,  
Eglin AFB, Florida,  
12-15 February 2001

MIT Lincoln Laboratory's  
Microelectronics Laboratory

C. L. Keast

Lincoln Laboratory  
Technical Seminar Series,  
University of Michigan,  
Ann Arbor, Michigan,  
23 February 2001

Controlled Contamination of Optics  
Under 157-nm Laser Irradiation

T. M. Bloomstein  
V. Liberman  
S. T. Palmacci  
M. Rothschild

SPIE Microlithography 2001,  
Santa Clara, California,  
25 February–2 March 2001

UV Cleaning of Contaminated  
157-nm Reticles

T. M. Bloomstein  
V. Liberman  
M. Rothschild  
N. N. Efremow  
D. E. Hardy  
S. T. Palmacci

SPIE Microlithography 2001,  
Santa Clara, California,  
25 February–2 March 2001

High Resolution Fluorocarbon  
Based Resist for 157-nm  
Lithography

T. H. Fedynyshyn  
R. R. Kunz  
R. F. Sinta  
M. Sworin  
W. A. Mowers  
R. B. Goodman  
S. P. Doran

SPIE Microlithography 2001,  
Santa Clara, California,  
25 February–2 March 2001

Investigation of Full-Field CD  
Control of Sub-100 nm Gates  
Produced by Phase-Shift 248 nm  
Lithography

M. Fritze  
B. Tyrrell  
D. Astolfi  
P. Davis  
B. Wheeler  
S. Cann  
D. Chan\*  
P. Rhyins\*  
M. Mastovich\*  
N. Sullivan\*  
R. Brandon\*

SPIE Microlithography 2001,  
Santa Clara, California,  
25 February–2 March 2001

100 nm Node Lithography with  
KrF?

M. Fritze  
B. Tyrrell  
D. Astolfi  
D. Yost  
P. Davis  
B. Wheeler  
S. Cann  
H. Y. Liu\*  
M. Ma\*  
D. Chan\*  
P. Rhyins\*  
C. Carney\*  
J. Ferri\*

SPIE Microlithography 2001,  
Santa Clara, California,  
25 February–2 March 2001

Photoresist Outgassing at 157 nm  
Exposure

R. R. Kunz  
T. M. Bloomstein  
S. Hien\*  
S. Basset\*

SPIE Microlithography 2001,  
Santa Clara, California,  
25 February–2 March 2001

Experimental VUV Absorbance  
Study of Fluorine-Functionalized  
Polystyrenes

R. R. Kunz  
R. Sinta  
M. Sworin  
T. H. Fedynyshyn  
V. Liberman  
J. E. Curtin

SPIE Microlithography 2001,  
Santa Clara, California,  
25 February–2 March 2001

---

\*Author not at Lincoln Laboratory.

Marathon Evaluation of Bulk  
Materials and Thin Film Coatings  
for 157-nm Lithography

V. Liberman  
M. Rothschild  
N. N. Efremow  
S. T. Palmacci  
J. H. C. Sedlacek  
C. VanPeski\*  
K. Orvek\*

SPIE Microlithography 2001,  
Santa Clara, California,  
25 February–2 March 2001

Spherically Deformed CCD  
Imagers for Passive Sensors

J. A. Gregory  
C. M. DeFranzo  
G. J. Swanson  
A. H. Loomis

Military Sensing Symposia  
Specialty Group on Passive  
Sensors,  
Vienna, Virginia  
5-7 March 2001

Hybrid Low-Light-Level CMOS  
Sensor Development

D. D. Rathman  
R. K. Reich  
D. M. O'Mara  
A. H. Loomis  
K. Pedrotti\*  
A. Joshi\*  
G. Hughes\*  
S. Galeema\*  
M. Buckley\*

Military Sensing Symposia  
Specialty Group on Passive  
Sensors,  
Vienna, Virginia  
5-7 March 2001

Orientation Dependence of  
GaInAsSb Grown by  
Organometallic Vapor Phase  
Epitaxy

C. A. Wang  
D. R. Calawa  
C. J. Vineis

10th Biennial Workshop on  
OMVPE,  
San Diego, California,  
11-15 March 2001

Determination of Free Carrier  
Concentration in *n*-Type GaSb  
Using Raman Spectroscopy

C. A. Wang  
D. C. Oakley  
J. E. Maslar\*  
W. S. Hurst\*

10th Biennial Workshop on  
OMVPE,  
San Diego, California,  
11-15 March 2001

Spontaneous Vertical Composition  
Modulation in Epitaxial GaInAsSb  
Grown on Vicinal Substrates

C. A. Wang  
C. J. Vineis  
D. R. Calawa  
P. M. Nitishin

10th Biennial Workshop on  
OMVPE,  
San Diego, California,  
11-15 March 2001

---

\*Author not at Lincoln Laboratory.

AlGaAsSb/GaSb Bragg Reflectors Grown by Organometallic Vapor Phase Epitaxy	C. A. Wang C. J. Vineis H. K. Choi	10th Biennial Workshop on OMVPE, San Diego, California, 11-15 March 2001
MIT Lincoln Laboratory: Physics and Technology in the National Interest	R. W. Ralston	American Physical Society Meeting, Seattle, Washington, 12-16 March 2001
High-Temperature Superconductors for Analog Signal Processing	T. C. L. G. Sollner	Lincoln Laboratory Technical Seminar Series, The Penn State University, University Park, Pennsylvania, 27 March 2001
Mobile Surface Electrons on Negative Electron Affinity Diamond	M. W. Geis	Lincoln Laboratory Technical Seminar Series, University of Maine, Orono, Maine, 28 March 2001
CCD Focal Plane Array for the Chandra X-ray Observatory	J. A. Gregory	Harvard Cyclotron Symposium, Cambridge, Massachusetts, 6 April 2001
Nanostructured Thermoelectric Materials and Devices	T. C. Harman P. J. Taylor M. P. Walsh B. E. LaForge	Advanced Thermoelectric Materials Conference, Warrenton, Virginia, 9-11 April 2001
CANARY Biosensor Development	M. A. Hollis	Lincoln Laboratory Technical Seminar Series, Virginia Polytechnic Institute and State University, Blacksburg, Virginia, 13 April 2001

Optical Sampling for High-Speed  
High-Resolution Analog-to-Digital  
Converters

P. W. Juodawlkis  
R. C. Williamson

IEEE Aerospace and Electronic  
Systems Meeting,  
Sudbury, Massachusetts,  
18 April 2001

Ferrite/Ferroelectric/  
Superconductor Resonator

D. E. Oates

American Ceramics Society,  
Indianapolis, Indiana,  
24 April 2001

Ferrite Material Investigation

D. E. Oates

American Ceramics Society,  
Indianapolis, Indiana,  
24 April 2001

## ORGANIZATION

### SOLID STATE DIVISION

D. C. Shaver, Head  
R. W. Ralston, Associate Head  
N. L. DeMeo, Jr., Assistant  
Z. J. Lemnios, Senior Staff  
  
J. W. Caunt, Assistant Staff  
K. J. Challberg, Administrative Staff  
J. D. Pendergast, Administrative Staff

#### SUBMICROMETER TECHNOLOGY

M. Rothschild, Leader  
T. M. Lyszczarz, Assistant Leader  
T. H. Fedynyshyn, Senior Staff  
R. R. Kunz, Senior Staff

Astolfi, D. K.  
Bloomstein, T. M.  
Cann, S. G.  
DiNatale, W. F.  
Efremow, N. N., Jr.  
Forte, A. R.  
Geis, M. W.  
Goodman, R. B.

Krohn, K. E.  
Lieberman, V.  
Mowers, W. A.  
Palmacci, S. T.  
Sedlacek, J. H. C.  
Spector, S. J.  
Switkes, M.  
Sworin, M.

#### QUANTUM ELECTRONICS

A. Sanchez-Rubio, Leader  
T. Y. Fan, Assistant Leader  
T. H. Jeys, Senior Staff  
J. J. Zayhowski, Senior Staff

Aggarwal, R. L.  
Daneu, J. L.  
Daneu, V.  
DiCecca, S.  
Goyal, A. K.

Herzog, W. D.  
Lynch, E. J.  
O'Brien, P. W.  
Ochoa, J. R.

#### ELECTRO-OPTICAL MATERIALS AND DEVICES

J. C. Twichell, Leader  
G. W. Turner, Assistant Leader  
D. L. Spears, Senior Staff  
C. A. Wang, Senior Staff  
R. C. Williamson, Senior Staff

Bailey, R. J.  
Betts, G. E.  
Calawa, D. R.  
Calawa, S. D.  
Connors, M. K.  
Donnelly, J. P.  
Goodhue, W. D.  
Hargreaves, J. J.  
Harman, T. C.

Harris, C. T.  
Huang, R. K.  
Juodawlkis, P. W.  
LaForge, B. E.  
Liau, Z. L.  
Mahoney, L. J.  
Manfra, M. J.  
McIntosh, K. A.  
Missaggia, L. J.

Molnar, R. J.  
Mull, D. E.  
Napoleone, A.  
Nitishin, P. M.  
Oakley, D. C.  
O'Donnell, F. J.  
Plant, J. J.  
Taylor, P. J.  
Younger, R. D.

#### BIOSENSOR AND MOLECULAR TECHNOLOGIES

M. A. Hollis, Leader

Blanchard, D. J.	Nargi, F. E.
Graves, C. A.	Parameswaran, L.
Harper, J. D.	Petrovick, M. S.
Mathews, R. H.	Rider, T. H.

#### ANALOG DEVICE TECHNOLOGY

T. C. L. G. Sollner, Leader  
L. M. Johnson, Assistant Leader  
A. C. Anderson, Senior Staff

Anthony, M. P.	Murphy, P. G.
Berggren, K. K.	Oates, D. E.
Boisvert, R. R.	Sage, J. P.
Fitch, G. L.	Santiago, D. D.
Kohler, E. J.	Seaver, M. M.
Lyons, W. G.	Slattery, R. L.
Macedo, E. M., Jr.	Weir, T. J.

#### ADVANCED IMAGING TECHNOLOGY

B. B. Kosicki, Leader  
R. K. Reich, Assistant Leader  
B. E. Burke, Senior Staff

Aull, B. F.	Johnson, K. F.
Ciampi, J. S.	Lind, T. A.
Cooper, M. J.	Loomis, A. H.
Craig, D. M.	McGonagle, W. H.
Daniels, P. J.	O'Mara, D. M.
Doherty, C. L., Jr.	Percival, K. A.
Dolat, V. S.	Rathman, D. D.
Felton, B. J.	Stern, A.
Gregory, J. A.	Young, D. J.

#### ADVANCED SILICON TECHNOLOGY

C. L. Keast, Leader  
V. Suntharalingam, Assistant Leader  
P. W. Wyatt, Senior Staff

Austin, E. E.	Newcomb, K. L.
Berger, R.	Rabe, S.
Bozler, C. O.	Soares, A. M.
Burns, J. A.	Travis, L.
Chen, C. K.	Tyrrell, B. M.
Chen, C. L.	Warner, K.
D'Onofrio, R. P.	Wheeler, B. D.
Fritze, M.	Yost, D.-R.
Gouker, P. M.	Young, G. R.
Knecht, J. M.	

# 1. QUANTUM ELECTRONICS

## 1.1 PERIODICALLY POLED BaMgF<sub>4</sub> FOR UV FREQUENCY GENERATION

The need exists for improved frequency conversion materials for uv and vacuum uv generation. Currently available materials, such as BBO, LBO, and CLBO, all have significant limitations including solarization, large walk-off under birefringent phase matching, limited vacuum uv transparency, and/or difficult handling because of being hygroscopic. Here, we report on ferroelectric domain inversion in BaMgF<sub>4</sub> (BMF). This material has transparency to <140 nm, is resistant to solarization, and can be used for quasi-phase-matched (QPM) interactions, which eliminates Poynting vector walk-off.

BMF is an orthorhombic (point group mm2), ferroelectric crystal that was originally investigated for its nonlinear optical properties in the 1970s [1]–[3]. It was known that BMF and its isomorph BaZnF<sub>4</sub> have good short-wavelength transparency, but the birefringence in these materials was too small to angle phase match any interactions to generate uv. However, the development of QPM techniques can enable short-wavelength generation using these materials.

The second-order nonlinear coefficients in BMF are relatively small, consistent with the large band gap and low refractive index (Miller's rule). The largest nonlinear coefficient is  $d_{32}$ , which has been reported previously, in two separate measurements, to have a magnitude of 0.085 relative to  $d_{36}$  of KDP [3] and 0.13 relative to  $d_{11}$  of SiO<sub>2</sub> [1], both measured using a 1.064- $\mu$ m laser. These values are equivalent to ~0.06 pm/V. This tensor element can be accessed using QPM techniques.

The BMF crystal was grown by the Czochralski technique in argon atmosphere and pulled at 1 mm/h. The stoichiometric starting mixture was pre-reacted, melted, and crystallized in a hydrofluorinator, using anhydrous hydrogen fluoride as a protective atmosphere. The purity of the BaF<sub>2</sub> and MgF<sub>2</sub> was 99.9%.

Optical characterization of this material has been performed in the <200-nm wavelength region. The external optical transmission and derived absorption coefficient are shown in Figure 1-1. The material is transparent to ~130 nm, a significantly shorter wavelength than the 170 nm reported previously [1]. We believe that the intrinsic absorption coefficient might be significantly smaller than that measured here, as cation impurities (from the relatively impure starting materials) can substantially increase optical absorption near the band edge. Optical damage testing was performed by irradiating a sample with 157-nm radiation at 2 mJ/cm<sup>2</sup>/pulse with 10-ns-long pulses [4]. No change in optical transmission was measured for  $>1.1 \times 10^9$  pulses. The refractive indices  $n_b$  and  $n_c$ , which are important for QPM using  $d_{32}$ , were measured by the method of minimum deviation to wavelengths as short as 157 nm [5]. The Sellmeier fits to the measured data are

$$n_b^2 = 2.07971 + \frac{0.006897}{\lambda^2 - 0.00914} \quad (1.1)$$



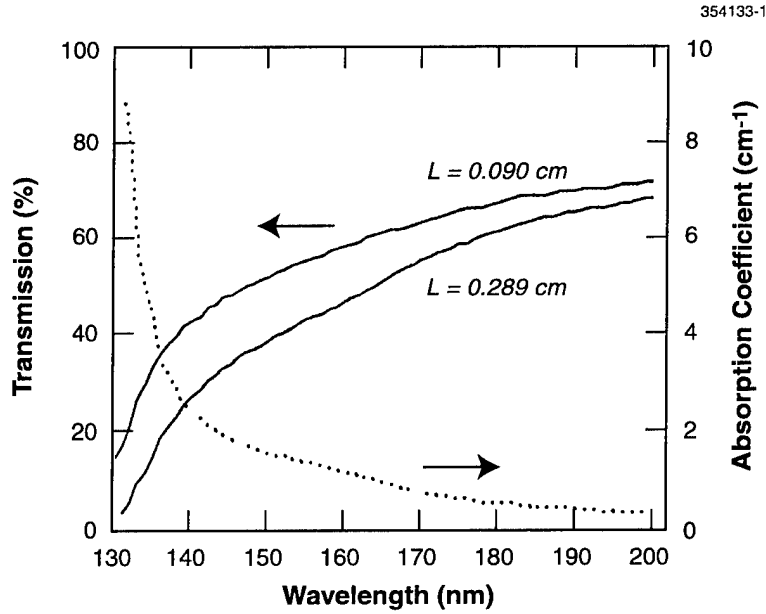


Figure 1-1. Transmission for two lengths of BaMgF<sub>4</sub> (BMF) and derived absorption coefficient.

$$n_c^2 = 2.12832 + \frac{0.0075537}{\lambda^2 - 0.008979} \quad (1.2)$$

where  $\lambda$  is the wavelength in units of microns. The estimated error in the refractive index measurements is on the order of  $\pm 0.0004$ , limited by the uncertainty in the apex angle of the prism.

Electric-field poling of BMF was performed using standard lithographic definition and high-voltage pulsing techniques on 500- $\mu\text{m}$ -thick wafers. The +c-face was lithographically patterned with a 19.2- $\mu\text{m}$ -period grating. The grating k-vector was parallel to the crystal a-axis. Sputtered NiCr was used for the electrode grating. The 9-mm-long, 4-mm-wide metal grating was overcoated with a 2- $\mu\text{m}$ -thick layer of photoresist with openings to contact the conducting LiCl solution. The bottom surface of the BMF was in direct contact with the solution, held in place with rubber O-rings. Poling was achieved with a series of 50-ms-long high-voltage pulses applied to a 220-k $\Omega$  series resistor, with a diode used to prevent back flow of current. The required poling fields were  $\sim 16$  kV/mm, which is about 0.75 that of LiNbO<sub>3</sub>. Figure 1-2 shows a scanning electron micrograph of a domain-inverted crystal with 20- $\mu\text{m}$  periods.

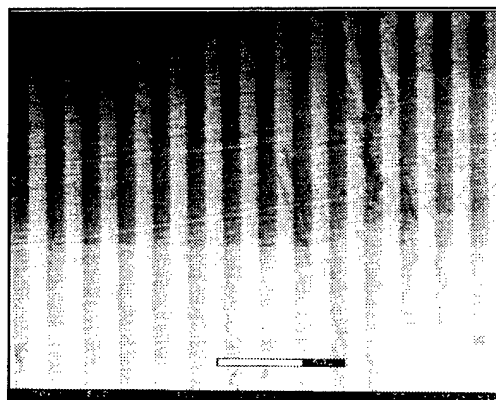


Figure 1-2. Periodically inverted domains in BMF visualized using an environmental scanning electron micrograph.

Reasonable conversion efficiency to the vacuum uv is expected in this material assuming first-order QPM. For frequency doubling to 157 nm, a conversion efficiency of 13% is projected in the plane-wave limit, assuming an incident fundamental intensity of  $1 \text{ GW/cm}^2$  and a converter length of 1 cm.

S. C. Buchter	A. Cassanho*
T. Y. Fan	H. P. Jenssen*
V. Liberman	E. J. Mason
J. J. Zayhowski	J. H. Burnett*
M. Rothschild	

## REFERENCES

1. J. G. Bergman, G. R. Crane, and H. Guggenheim, *J. Appl. Phys.* **46**, 4645 (1975).
2. K. Recker, F. Wallerfen, and S. Haussueh, *J. Cryst. Growth* **26**, 97 (1974).
3. F. S. Bechthold and S. Hassueh, *Appl. Phys.* **14**, 403 (1977).
4. V. Liberman, M. Rothschild, J. H. C. Sedlacek, R. S. Uttaro, A. K. Bates, and K. Orvek, *Proc. SPIE* **4000**, 488 (2000).
5. J. H. Burnett, R. Gupta, and U. Griesmann, *Proc. SPIE* **4000**, 1503 (2000).

---

\*Author not at Lincoln Laboratory.

## 2. ELECTRO-OPTICAL MATERIALS AND DEVICES

### 2.1 SENSITIVITY-BANDWIDTH PRODUCT FOR ELECTRO-OPTIC MODULATORS

For many applications in optical communications and signal processing, a great need exists for increasing the sensitivity of optical modulators. Higher sensitivity means lower drive power in some applications such as optical switching and lower electrical-to-optical loss and improved noise figure in other applications such as analog fiber-optic links [1]. For electro-optic modulators, the sensitivity is often characterized by the parameter  $V_\pi$ , which is the voltage required to cause a shift of 180 degrees in the phase  $\phi$  of an optical signal traversing the modulator. The goal is to reduce  $V_\pi$  or, equivalently, to increase  $\partial\phi/\partial V$ , where  $V$  is the applied voltage. Various approaches have included the search for materials with higher electro-optic coefficients, for geometries with better coupling of the electric field to the optical wave, and for special structures to enhance the phase sensitivity  $\partial\phi/\partial V$ . Recently, several proposals have been made to use optically resonant structures to increase the phase sensitivity (see, for example, [2]–[4]). However, the use of special structures carries with it some inherent bandwidth limitations, which are the subject of this report.

The simple case of a lumped-element nondispersive (optical index constant vs wavelength) electro-optic modulator illustrates the basic tradeoff, as seen in Figure 2-1. For a modulator of length  $L$ , the optical time delay  $T$  through the modulator is given by  $T = L n/c$ , where  $n$  is the optical index. The lumped-element assumption is equivalent to invoking an electrode geometry such that an applied voltage changes the effective index  $n$  for an optical wave propagating uniformly over the region indicated. This situation is closely approached for an electro-optic modulator in which the modulating voltage is applied broadside to electrodes running along the path of the optical wave. The voltage-induced phase shift  $\phi(\omega, V)$  is a function of both optical frequency and applied voltage. The phase shift  $\phi = \omega L n/c$ . It is straightforward to show that

$$\partial\phi/\partial V = (dn/dV)(\omega/n)T \quad (2.1)$$

The more time  $T$  that the optical wave spends in the region of altered index, the larger will be the resulting phase shift.

For a lumped-element modulator, changes in the optical index that occur while the optical wave is transiting the modulator will be averaged over the propagation path and thus limit the bandwidth of the modulation that can be imposed on the light wave. In general, the bandwidth  $\Delta\omega$  of the electro-optic modulation is equal to  $T^{-1}$ . Accordingly,

$$(\partial\phi/\partial V)\Delta\omega = (dn/dV)(\omega/n) \quad (2.2)$$

Equation (2.2) implies a fundamental sensitivity-bandwidth product for lumped-element modulators. For a given material, the magnitude of  $dn/dV$  is usually optimized by the choice of the optical waveguide and the electrode structure so as to maximize the overlap of the fields of the optical wave with the applied electrical field. Once  $dn/dV$  is optimized, there is a constant sensitivity-bandwidth product. The only way to increase the sensitivity-bandwidth product for a lumped-element modulator is to use a better electro-optic material. Note that in Equation (2.2),  $V$  is the voltage on the modulator electrodes. The circuit effects of the coupling of an electronic driver to the electrodes are not included.

These arguments apply to a simple nondispersive optical path. It is less obvious that Equations (2.1) and (2.2) also apply to much more complicated geometries, including those with resonant optical structures. In those situations, Equation (2.1) is applicable when  $T$  is set equal to  $T_g$ , the optical group delay. This relationship directly follows from the assumption that the system shown in the box in Figure 2-1 is linear. The optical response of the system can be characterized by an impulse response of the form  $h(t n/n_o)$ , where  $h(t)$  is the impulse response when the index is equal to  $n_o$ . A change in index uniformly stretches or contracts the impulse response. For simplicity, it is assumed that the index is constant with respect to  $\omega$ . The effects of weak dispersion only slightly modify the conclusions.

The phase  $\phi(\omega, n)$  of the frequency-domain transfer function is given by

$$\phi(\omega, n) = \arctan[\text{Im } H(\omega, n) / \text{Re } H(\omega, n)] \quad (2.3)$$

where  $H(\omega, n)$  is the Fourier transform of  $h(t n/n_o)$ . By taking partial derivatives of  $\phi$  with respect to  $\omega$  and  $n$ , a simple relationship results:

$$\partial\phi/\partial n = (\omega/n)(\partial\phi/\partial\omega) = (\omega/n)T_g \quad (2.4)$$

This expression directly implies Equations (2.1) and (2.2).

Figure 2-2 shows three configurations for guided-optical-wave electro-optic modulators that have been considered as possible means for enhancing the sensitivity of modulators. The first, shown in Figure 2-2(a), is a chirped reflection grating. This geometry is initially appealing because a change in index moves the effective reflection point along the grating, thus possibly providing a means of enhancing  $\partial\phi/\partial n$ . However, Equation (2.4) indicates that the sensitivity is directly related to the delay from the input to the resonantly reflecting region and back out. The sensitivity is the same as that achieved by placing a broadband reflector at the position of the resonant reflection. The chirped grating provides no sensitivity enhancement. The chirp does yield a second-order quadratic change of phase with respect to index that is likely more troublesome than useful.

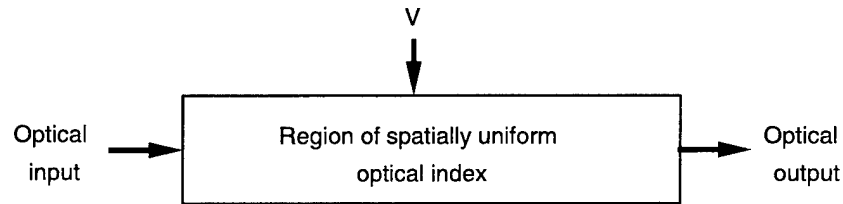


Figure 2-1 Lumped-element electro-optic modulator in which the region indicated has a spatially uniform index varied through the application of voltage  $V$ .

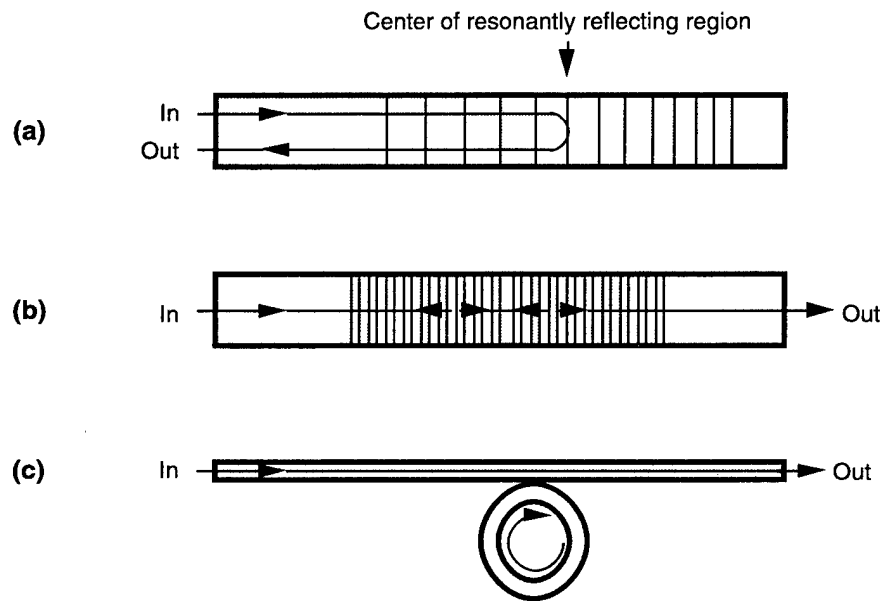


Figure 2-2. Guided-optical structures with dispersive propagation paths: (a) chirped grating reflector, (b) Fabry-Perot resonator with grating reflectors, (c) side-coupled resonant ring.

Figures 2-2(b) and 2-2(c) show optically resonant structures, a Fabry-Perot resonator with grating reflectors and a resonant ring. At the resonant optical frequency, the optical wave dwells for a time  $T_g$  in the region of changing optical index, and the sensitivity is enhanced as indicated by Equations (2.1), (2.2), and (2.4). However, a fundamental sensitivity-bandwidth limit is imposed. As compared to a simple nondispersive delay path, the advantage of the resonant geometries is that for the same sensitivity, the region of varying index can be made smaller. This means a lower capacitance for the electrodes and a more favorable input impedance for the electrical drive.

In order to maximize the bandwidth of electro-optic modulators, it is necessary to employ traveling-wave geometries in which optical and electrical waves are launched collinearly (see, for example, [5] and [6]). In this situation, the index varies in time and space along the optical path and thus Equations (2.1)–(2.4) do not apply. Matching of the velocity of the optical and electrical waves is important for wideband operation. In general, the sensitivity of the modulator will be lower than if the same basic geometry were employed for low-bandwidth modulation. For traveling-wave modulators, the relationship equivalent to Equation (2.1) becomes

$$\partial\phi/\partial V \leq (dn/dV)_{\max} (\omega/n) T_g \quad (2.5)$$

where  $(dn/dV)_{\max}$  is the maximum value of the index modulation along the optical propagation path and  $T_g$  is the optical delay from input to output. There is no inherent sensitivity-bandwidth tradeoff for this type of modulator. If good velocity matching is achieved, sensitivity is enhanced by making the modulator longer. However, the loss of the electrical signal as it travels through the modulator becomes an important consideration that eventually limits the sensitivity. Equation (2.5) sets an upper limit on the sensitivity of a traveling-wave modulator. Gratings [7] or other structures to modify and better match the group velocities of the optical and electrical waves may be of use in better approaching the upper limit set by Equation (2.5).

R. C. Williamson

## 2.2 EFFECT OF SUBSTRATE ORIENTATION ON PHASE SEPARATION IN EPITAXIAL GaInAsSb

$\text{Ga}_{1-x}\text{In}_x\text{As}_y\text{Sb}_{1-y}$  alloys can be grown lattice matched to GaSb or InAs substrates and are useful for a wide range of optoelectronic devices operating in the mid-infrared wavelength region [8]–[10]. The existence of a large miscibility gap, however, limits the material quality of alloys with  $x$  and  $y$  values that are in the range between approximately 0.15 and 0.85 [11],[12], and phase separation by spinodal decomposition is likely to occur. Microscopic compositional inhomogeneities consisting of GaAs- and

InSb-rich phases were observed in  $\text{Ga}_{1-x}\text{In}_x\text{As}_y\text{Sb}_{1-y}$  grown by organometallic vapor phase epitaxy (OMVPE) [13],[14]. As a result, the optical, structural, and electrical properties were degraded by phase separation [14]–[17]. In this report, the effect of the substrate miscut direction on  $\text{Ga}_{1-x}\text{In}_x\text{As}_y\text{Sb}_{1-y}$  grown nominally lattice matched to GaSb substrates by OMVPE is reported.

$\text{Ga}_{1-x}\text{In}_x\text{As}_y\text{Sb}_{1-y}$  epitaxial layers were grown nominally lattice matched to vicinal (001) Te-doped GaSb substrates with miscut angles of 2 or 6°  $\rightarrow$  (-1-11)A, (1-11)B, or (101). Solution trimethylindium, triethylgallium, tertiarybutylarsine, and trimethylantimony were used as precursors as described previously [15]. Layers with alloy compositions  $0.1 \leq x \leq 0.19$ ,  $0.09 \leq y \leq 0.17$  were grown, with the larger  $x$  and  $y$  values representing alloys deeper in the miscibility gap [11],[12]. The growth temperature was 575°C. Although previous results reported a smaller extent of phase separation for growth at a low temperature of 525°C [15], this higher temperature was used to promote a step-bunched surface, which was reported to enhance phase separation [17]. The layers were typically 1–2  $\mu\text{m}$  in thickness and grown at  $\sim 5 \mu\text{m/h}$ . A vertical rotating-disk OMVPE reactor was used with  $\text{H}_2$  carrier gas at a flow rate of 10 slpm, reactor pressure of 150 Torr, and typical rotation rate of 40 rpm.

The layers were characterized with atomic force microscopy (AFM) operated in tapping mode. Etched Si cantilevers with a nominal tip radius of 5–10 nm and a sidewall angle of 10° were used. The structural quality was evaluated by high-resolution x-ray diffraction (HRXRD), while photoluminescence (PL) measurements at 4 and 300 K were used to characterize the optical properties.

Figure 2-3 shows AFM images of  $\text{Ga}_{1-x}\text{In}_x\text{As}_y\text{Sb}_{1-y}$  layers with two nominally different alloy compositions grown on (001) 2°  $\rightarrow$  (-1-11)A, (001) 2°  $\rightarrow$  (1-11)B, and (001) 2°  $\rightarrow$  (101) substrates. The alloy composition was estimated from XRD and 300-K PL. AFM images of layers with  $x \sim 0.1$  and  $y \sim 0.09$ , which corresponds to  $\sim 2.1\text{-}\mu\text{m}$  GaInAsSb, are shown in Figures 2-3(a), 2-3(b), and 2-3(c). All surfaces exhibit a periodic morphology that is attributed to step-bunching [18],[19]. The step edges are aligned perpendicular to the miscut direction and terraces extend over hundreds of nanometers. The average width of (001) terraces vary from about 38, 29, and 40 nm for the (001) 2°  $\rightarrow$  (-1-11)A, (001) 2°  $\rightarrow$  (1-11)B, and (001) 2°  $\rightarrow$  (101) substrates, respectively, and step heights vary accordingly to preserve the substrate miscut angle of about 2°. Larger-scale height undulations with a periodicity of about 150 nm are observed for layers grown on the (001) 2°  $\rightarrow$  (1-11)B and (001) 2°  $\rightarrow$  (101) substrates. These undulations are not always present [16]–[17], and are related to a vertical composition modulation that is tilted with respect to the substrate surface [20].

AFM images of layers with higher alloy composition,  $0.16 \leq x \leq 0.19$ ,  $0.14 \leq y \leq 0.17$ , are shown in Figures 2-3(d), 2-3(e), and 2-3(f). The 300-K PL emission corresponds to 2.4  $\mu\text{m}$  for the samples in Figures 2-3(d) and 2-3(e), and 2.3  $\mu\text{m}$  for that in Figure 2-3(f). The layers are at various stages in breakdown of the surface structure, where the step edges are wavy and the long step-bunches have broken up into an irregular morphology. Such morphology is indicative of phase separation during epitaxial growth [16]–[17]. The miscut direction of the original substrate is evident only for the layers grown on (001) 2°  $\rightarrow$  (-1-11)A and (001) 2°  $\rightarrow$  (1-11)B substrates. GaInAsSb grown on (001) 2°  $\rightarrow$  (101) exhibits

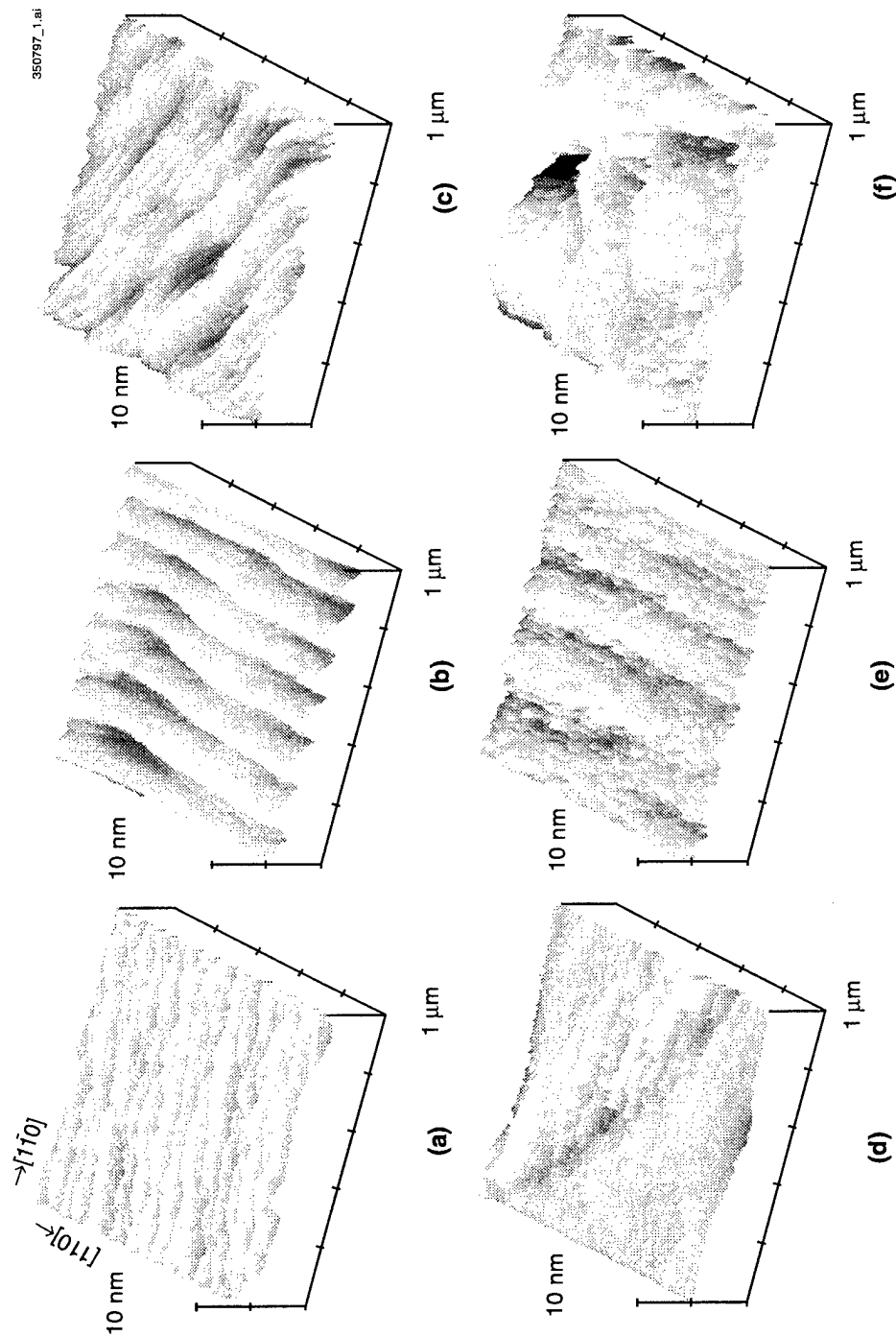


Figure 2-3. Atomic force microscope images of (a)  $Ga_{0.9}In_{0.1}As_{0.09}Sb_{0.91}$  on  $(001) 2^\circ \rightarrow (-1-11)A$ , (b)  $Ga_{0.9}In_{0.1}As_{0.09}Sb_{0.91}$  on  $(001) 2^\circ \rightarrow (1-11)B$ , (c)  $Ga_{0.9}In_{0.1}As_{0.09}Sb_{0.91}$  on  $(001) 2^\circ \rightarrow (101)$ , (d)  $Ga_{0.82}In_{0.18}As_{0.16}Sb_{0.84}$  on  $(001) 2^\circ \rightarrow (-1-11)A$ , (e)  $Ga_{0.81}In_{0.19}As_{0.17}Sb_{0.83}$  on  $(001) 2^\circ \rightarrow (1-11)B$ , and (f)  $Ga_{0.84}In_{0.16}As_{0.14}Sb_{0.86}$  on  $(001) 2^\circ \rightarrow (101)$ . Vertical scale is 5 nm/division in all cases.



relatively large (100–500 nm) flat regions separated by narrow trenches that are several nanometers deep and aligned nearly parallel with  $[-110]$ . Previously, it was reported that compared to the average composition, these narrow trenches corresponded to regions that were as much as 2–3 at.% GaAs-rich, while the larger regions were InSb-rich [13],[14].

Figure 2-4 shows HRXRD reciprocal space maps of  $\text{Ga}_{0.9}\text{In}_{0.1}\text{As}_{0.09}\text{Sb}_{0.91}$  grown on  $(001) 2^\circ \rightarrow (1-11)\text{B}$  and  $\text{Ga}_{1-x}\text{In}_x\text{As}_y\text{Sb}_{1-y}$  with  $0.16 \leq x \leq 0.19$ ,  $0.14 \leq y \leq 0.17$  on substrates with the three different miscut directions. HRXRD of  $\text{Ga}_{0.9}\text{In}_{0.1}\text{As}_{0.09}\text{Sb}_{0.91}$  grown on  $(001) 2^\circ \rightarrow (-1-11)\text{A}$  and  $(001) 2^\circ \rightarrow (101)$  substrates are similar to that on  $(001) 2^\circ \rightarrow (1-11)\text{B}$ , as shown in Figure 2-4(a). All layers are nominally lattice matched to the GaSb substrate. Varying degrees of strain exist, however, owing to lattice constant variations and epitaxial tilt. Both strain and tilt are negligible for the  $\text{Ga}_{0.9}\text{In}_{0.1}\text{As}_{0.09}\text{Sb}_{0.91}$  layer. On the other hand,  $\text{Ga}_{1-x}\text{In}_x\text{As}_y\text{Sb}_{1-y}$  layers with  $0.16 \leq x \leq 0.19$ ,  $0.14 \leq y \leq 0.17$  are extremely inhomogeneous. Compressive and tensile strain, which is associated with GaAs-rich and InSb-rich quaternaries resulting from phase separation, gives rise to lattice constant variation (y-axis) and tilt (x-axis). GaInAsSb grown on  $(001) 2^\circ \rightarrow (1-11)\text{B}$  exhibits the smallest tilt and narrowest range of lattice constant, while these parameters increase for  $(001) 2^\circ \rightarrow (-1-11)\text{A}$  and further still for  $(001) 2^\circ \rightarrow (101)$ .

The 4- and 300-K PL spectra of  $\text{Ga}_{0.9}\text{In}_{0.1}\text{As}_{0.09}\text{Sb}_{0.91}$  grown on  $(001) 2^\circ \rightarrow (1-11)\text{B}$  are shown in Figure 2-5(a). The PL spectra of  $\text{Ga}_{0.9}\text{In}_{0.1}\text{As}_{0.09}\text{Sb}_{0.91}$  grown on  $(001) 2^\circ \rightarrow (-1-11)\text{A}$  and  $(001) 2^\circ \rightarrow (101)$  substrates are similar, and Table 2-1 summarizes the PL data for those samples shown in Figures 2-3(a)–2-3(c). The 4-K PL full width at half-maximum (FWHM) value provides a semiquantitative measure of the degree of phase separation [16],[21]: values increase with phase separation. The FWHM values are 9.0, 7.2, and 9.3 meV for  $(001) 2^\circ \rightarrow (-1-11)\text{A}$ ,  $(1-11)\text{B}$ , and  $(101)$  substrates, respectively. Thus, these results indicate that the most homogeneous alloy is obtained for the layer grown on  $(001) 2^\circ \rightarrow (1-11)\text{B}$ , while similar quality is obtained for layers grown on  $(001) 2^\circ \rightarrow (-1-11)\text{A}$  and  $(001) 2^\circ \rightarrow (101)$ . All samples show a difference between the 4- and 300-K PL peak energy ( $E_{4-300\text{K}}$ ) of  $\sim 74$  meV, which corresponds to the expected difference based on the energy gap dependence on temperature.

Table 2-1 also lists PL data of  $\text{Ga}_{0.9}\text{In}_{0.1}\text{As}_{0.09}\text{Sb}_{0.91}$  grown on substrates with a  $6^\circ$  miscut angle in the three different miscut directions. In all cases, the 4-K PL FWHM values are smaller for layers grown with the larger miscut angle. AFM measurements indicated that terrace widths are typically smaller in the range between 15 and 25 nm for layers grown on the  $6^\circ$  miscut substrates.

The 4- and 300-K PL spectra of  $\text{Ga}_{1-x}\text{In}_x\text{As}_y\text{Sb}_{1-y}$  layers with  $0.16 \leq x \leq 0.19$ ,  $0.14 \leq y \leq 0.17$  are shown in Figures 2-5(b)–2-5(d) and the data are summarized in Table 2-1. The 4-K PL FWHM values are considerably larger at 36.1, 13.6, and 42.0 meV for layers on  $(001) 2^\circ \rightarrow (-1-11)\text{A}$ ,  $(001) 2^\circ \rightarrow (1-11)\text{B}$ , and  $(001) 2^\circ \rightarrow (101)$  substrates, respectively. Band tailing is especially significant for layers grown on  $(001) 2^\circ \rightarrow (-1-11)\text{A}$  and  $(001) 2^\circ \rightarrow (101)$  substrates. The PL properties of  $\text{Ga}_{0.81}\text{In}_{0.19}\text{As}_{0.17}\text{Sb}_{0.83}$  grown on  $(001) 2^\circ \rightarrow (1-11)\text{B}$ , which also has the highest  $x$  and  $y$  values, are significantly better.  $E_{4-300\text{K}}$  is 68 meV for this substrate miscut, compared to only about 18 meV for  $(001) 2^\circ \rightarrow (-1-11)\text{A}$  and  $(001) 2^\circ \rightarrow (101)$ . The red shift of 4-K PL spectra is due to recombination in the smaller-band-gap InSb-rich regions.

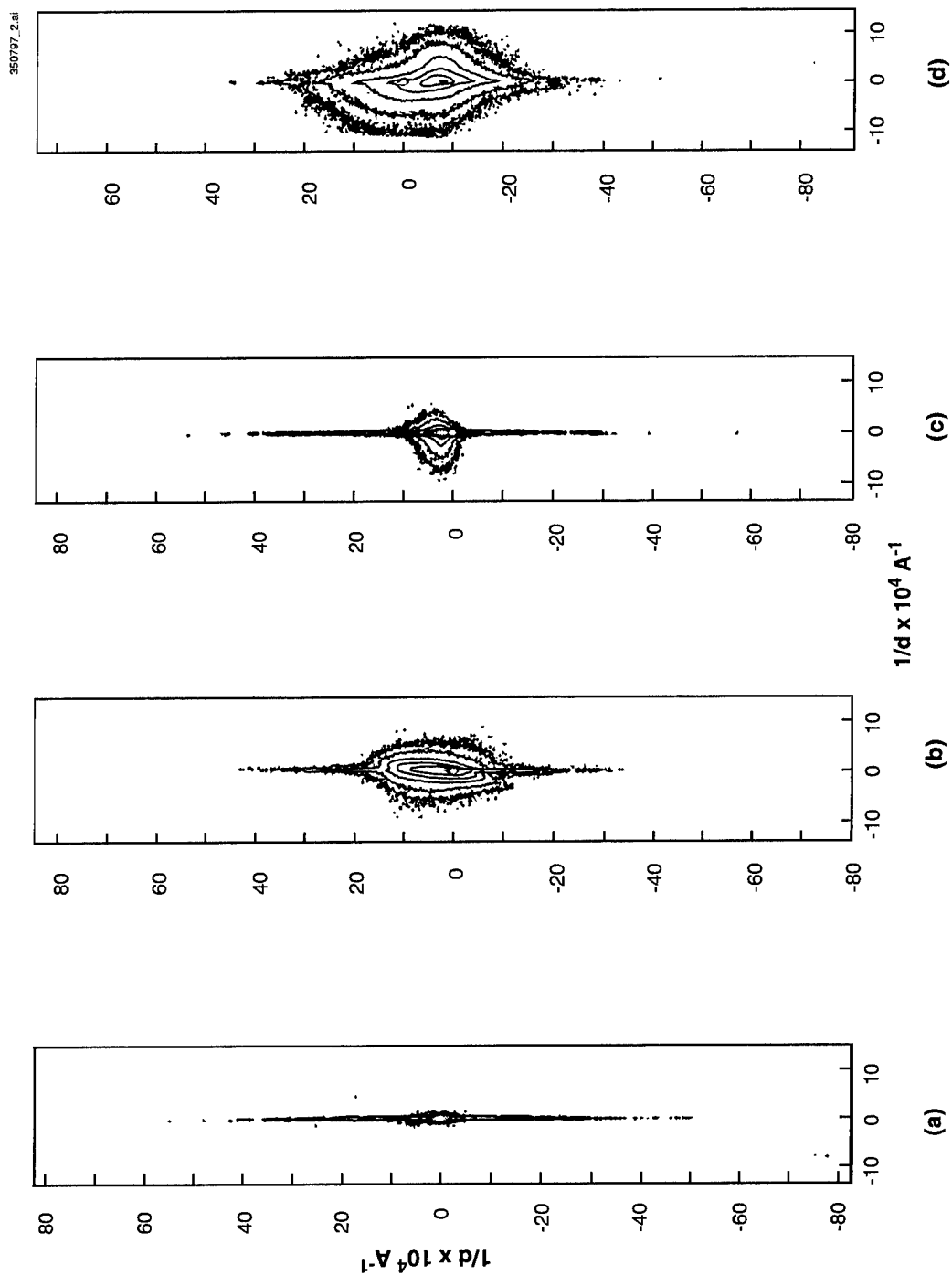


Figure 2-4. High-resolution x-ray diffraction of (a)  $\text{Ga}_{0.82}\text{In}_{0.18}\text{Sb}_{0.84}$  on  $(001) 2^\circ \rightarrow (-1-11)\text{A}$ , (b)  $\text{Ga}_{0.84}\text{In}_{0.16}\text{As}_{0.14}\text{Sb}_{0.86}$  on  $(001) 2^\circ \rightarrow (101)$ , (c)  $\text{Ga}_{0.82}\text{In}_{0.18}\text{As}_{0.16}\text{Sb}_{0.84}$  on  $(001) 2^\circ \rightarrow (-1-11)\text{A}$ , and (d)  $\text{Ga}_{0.84}\text{In}_{0.16}\text{As}_{0.14}\text{Sb}_{0.86}$  on  $(001) 2^\circ \rightarrow (1-11)\text{B}$ .

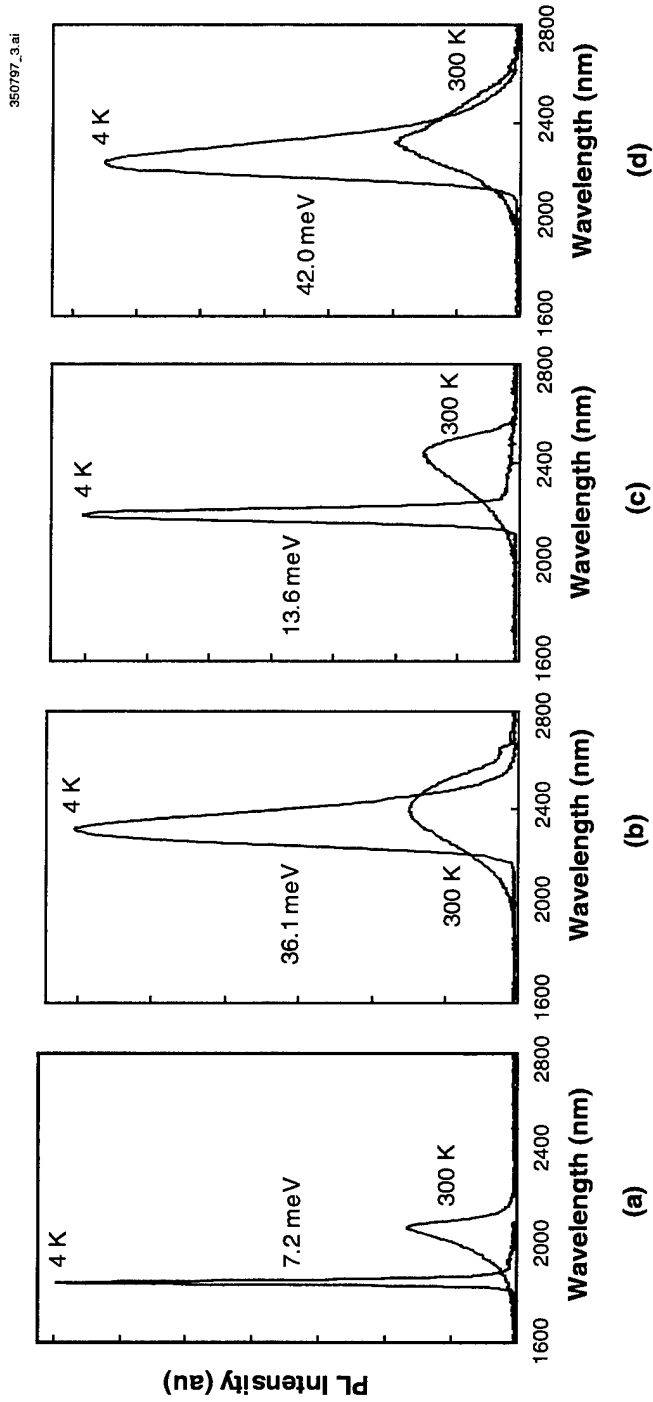


Figure 2-5. Photoluminescence spectra measured at 4 and 300 K of (a)  $\text{Ga}_{0.9}\text{In}_{0.1}\text{As}_{0.09}\text{Sb}_{0.91}$  on  $(001) 2^\circ \rightarrow (1-11)\text{B}$ , (b)  $\text{Ga}_{0.82}\text{In}_{0.18}\text{As}_{0.16}\text{Sb}_{0.84}$  on  $(001) 2^\circ \rightarrow (-1-11)\text{A}$ , (c)  $\text{Ga}_{0.81}\text{In}_{0.19}\text{As}_{0.17}\text{Sb}_{0.83}$  on  $(001) 2^\circ \rightarrow (1-11)\text{B}$ , and (d)  $\text{Ga}_{0.84}\text{In}_{0.16}\text{As}_{0.14}\text{Sb}_{0.86}$  on  $(001) 2^\circ \rightarrow (101)$ .

**TABLE 2-1**  
**Photoluminescence Data of GaInAsSb**

Substrate	300-K PL (nm)	4-K PL (nm)	E <sub>4-300K</sub> (meV)	4-K PL FWHM (meV)
(001) 2° → (-1-11)A	2088	1856	74.2	9.0
(001) 2° → (1-11)B	2080	1849	74.5	7.2
(001) 2° → (101)	2088	1858	73.5	9.3
(001) 2° → (-1-11)A	2397	2313	1.9	36.1
(001) 2° → (1-11)B	2441	2192	57.7	13.6
(001) 2° → (101)	2315	2238	1.8	42.0
(001) 6° → (-1-11)A	2090	1860	73.4	5.7
(001) 6° → (1-11)B	2082	1857	72.2	6.1
(001) 6° → (101)	2065	1844	72.0	5.8

Phase separation has been reported to proceed on the surface during epitaxial growth, and thus is sensitive to kinetic factors including temperature, adatom flux, and substrate surface orientation [14]–[17],[22]–[23]. The differences observed in the extent of phase separation on substrates with various misorientations are due to the different adatom incorporation rates. It is expected that as the rate of adatom incorporation at step edges increases, adatom clustering on (001) terraces is reduced, and thus phase separation is reduced. Step edges of substrates miscut toward (-1-11)A are terminated with group III atoms, A-steps, while substrates miscut toward (1-11)B are terminated with group V atoms, B-steps. Substrates miscut toward (101) have an equal density of A- and B-steps.

The AFM results suggest that adatom diffusion lengths are dependent on substrate miscut angle and direction. Substrates with a larger miscut angle have smaller terrace widths. Layers grown on (001) substrates miscut toward (1-11)B have the smallest terrace widths and (001) substrates miscut toward (101) have the largest. Consequently, GaInAsSb grown on substrates with a 6° miscut angle have better PL properties than those on substrates with a 2° miscut angle. In addition, layers grown on (001) substrates miscut toward (1-11)B have the least phase separation while (001) substrates miscut toward (101) have the most.

Although the exact nature of atomic bonding and reconstructions are unknown for GaSb-based materials grown by OMVPE, especially at step edges, the present results indicate that there is preferential incorporation of adatoms at B-step edges. This result is consistent with previous reports that the Ga sticking coefficient was higher for GaSb grown on substrates miscut toward the B surface compared to those toward the A surface [24], and is consistent with the mechanism proposed by Asai under low group V overpressure [25].

However, this mechanism does not explain the results for (001) substrates miscut toward (101) since these have both A- and B-step edges. Thus, an additional factor that may be important is the surface diffusion rate. The AFM image shown in Figure 2-3(f) indicates a surface structure with trenches aligned in the  $[-110]$  direction. These trenches are associated with GaAs-rich regions, and stronger composition modulation is observed along the  $[110]$ . Therefore, the adatom diffusion length is larger in the  $[110]$  direction compared to  $[-110]$  on the (001) surface [26]. If the limiting factor is diffusion along  $[110]$ , the diffusion length on (001)  $2^\circ \rightarrow (101)$  substrates would be longer by the square root of 2. The extent of phase separation is largest on these substrates.

In summary, the miscut direction of (001) GaSb substrates is an important parameter in determining the extent of phase separation, and thus epilayer quality, of GaInAsSb grown by OMVPE. Alloy decomposition results in microscopic compositional variations that increase in magnitude and ultimately leads to irregular surface step structure and degradation of structural and optical properties. These properties degrade as the extent of phase separation increases. Phase separation is more limited for GaInAsSb layers grown on (001)  $2^\circ \rightarrow (1-11)B$  substrates, which are consistently more homogeneous compared to layers of similar composition grown on (001)  $2^\circ \rightarrow (-1-11)A$  or (001)  $2^\circ \rightarrow (101)$  substrates. These results can be explained by the smaller adatom diffusion length on (001)  $2^\circ \rightarrow (1-11)B$  substrates.

C. A. Wang                      D. R. Calawa  
J. W. Chludzinski      D. C. Oakley

## REFERENCES

1. E. I. Ackerman, C. Cox III, G. Betts, H. Roussel, F. O'Donnell, and K. Ray, *IEEE Trans. Microwave Theory Tech.* **46**, 2025 (1998).
2. Y. Kokobun, S. Kubota, and S. T. Chu, *Electron. Lett.* **37**, 90 (2001).
3. M. K. Chin and S. T. Ho, *J. Lightwave Technol.* **16**, 1433 (1998).
4. W. J. Wang, S. Honkanen, S. I. Najafi, and A. Tervonen, *Proc. SPIE* **1794**, 366 (1993).
5. M. Koshiba, Y. Tsuji, and M. Nishio, *IEEE Trans. Microwave Theory Tech.* **47**, 1627 (1999).
6. W-K. Wang, R. W. Smith, and P. J. Anthony, *J. Lightwave Technol.* **13**, 2250 (1995).

7. J. B. Khurgin, J. U. Kang, and Y. J. Ding, *Opt. Lett.* **25**, 70 (2000).
8. Y. Tian, B. Zhang, T. Zhou, H. Jiang, and Y. Jin, *Phys. Status Solidi A* **174**, 413 (1999).
9. D. Garbuzov, M. Maiorov, H. Lee, V. Khalfin, R. Martinelli, and J. Connolly, *Appl. Phys. Lett.* **74**, 2990 (1999).
10. G. W. Charache, P. F. Baldasaro, L. R. Danielson, D. M. Depoy, M. J. Freeman, C. A. Wang, H. K. Choi, D. Z. Garbuzov, R. U. Martinelli, V. Khalfin, S. Saroop, J. M. Borrego, and R. J. Gutman, *J. Appl. Phys.* **85**, 2247 (1999).
11. M. J. Cherng, H. R. Jen, C. A. Larsen, G. B. Stringfellow, H. Lundt, and P. C. Taylor, *J. Cryst. Growth* **77**, 408 (1986).
12. K. Onabe, *Jpn. J. Appl. Phys.* **21**, L323 (1982).
13. C. A. Wang, H. K. Choi, S. L. Ransom, G. W. Charache, L. R. Danielson, and D. M. DePoy, *Appl. Phys. Lett.* **75**, 1305 (1999).
14. C. A. Wang, D. R. Calawa, and C. J. Vineis, to be published in *J. Cryst. Growth*.
15. C. A. Wang, H. K. Choi, and G. W. Charache, *IEEE Proc. J, Optoelectron.* **147**, 193 (2000).
16. C. A. Wang, *Appl. Phys. Lett.* **76**, 2077 (2000).
17. C. A. Wang, *J. Electron. Mater.* **29**, 112 (2000).
18. M. Kasu and N. Kobayashi, *Appl. Phys. Lett.* **62**, 1262 (1993).
19. M. Shinohara and N. Inoue, *Appl. Phys. Lett.* **66**, 1936 (1995).
20. C. A. Wang, C. J. Vineis, D. R. Calawa, and P. M. Nitishin, presented at the Fall Meeting of the Materials Research Society, Boston, Mass., 27 November–1 December 2000.
21. R. R. LaPierre, T. Okada, B. J. Robinson, D. A. Thompson, and G. C. Weatherly, *J. Cryst. Growth* **155**, 1 (1995).
22. T. L. McDevitt, S. Mahajan, D. E. Laughlin, W. A. Bonner, and V. G. Keramidas, *Phys. Rev. B* **45**, 6614 (1992).
23. R. R. LaPierre, B. J. Robinson, and D. A. Thompson, *Appl. Surf. Sci.* **90**, 437 (1995).
24. N. Bertru, M. Nouaoura, J. Bonnet, and L. Lassabatere, *J. Cryst. Growth* **160**, 1 (1996).
25. H. Asai, *J. Cryst. Growth* **80**, 425 (1987).
26. J.-S. Liu, J.-S. Wang, K.Y. Hsieh, and H.-H. Lin, *J. Cryst. Growth* **206**, 15 (1999).

### 3. SUBMICROMETER TECHNOLOGY

#### 3.1 ORGANIC PELLICLE MEMBRANES FOR 157-nm LITHOGRAPHY

Lithography utilizing 157-nm lasers has been embraced by the major semiconductor manufacturers as the next, and possibly last, technology generation utilizing light for device fabrication. This technology is expected to go into production by 2004 for the 90-nm node [1]. Under a Cooperative Research and Development Agreement with SEMATECH, we have been investigating pellicle materials for 157-nm lithography.

In order to reduce the number of particle defects on a reticle for a projection system, a protective pellicle film is applied to a frame attached over the reticle. The cover is positioned a few millimeters away from the reticle surface so that particles landing on the cover will be out of the focal plane of the projection optics. Traditionally, pellicles used for 248- and 193-nm wavelength lithography have been organic fluoropolymer membranes with a thickness range between 0.5 and 1  $\mu\text{m}$ . A thin pellicle membrane has a number of advantages. First, it will not act as an optical element that could introduce unnecessary complexity to the system. Second, since its thickness is within the coherence length of the source, optimizing the pellicle thickness can eliminate reflective losses via an etalon effect. For example, the transmissivity of 193-nm fluoropolymer pellicle materials can be above 99% for micron-range thicknesses [2]. Owing to lower utilization of reticles as compared to the projection optics, the durability requirements of pellicle materials are less stringent. The material is expected to have an initial transmission above 98% and retain a final transmission of 97% after a laser dose of  $60 \times 10^6$  pulses at  $0.1 \text{ mJ/cm}^2/\text{pulse}$ .

For 157-nm applications, the choice of transparent organic materials is limited, as most conventional 193-nm pellicle materials become absorbing. However, a host of new fluorocarbon polymers have been synthesized recently, with transparencies approaching 95% at 157 nm for 1- $\mu\text{m}$ -thick films. Here, we present initial results on the durability of such new materials under lamp- and laser-irradiation.

At 157-nm wavelength, measurement results are very sensitive to airborne contamination that deposits on the sample. For this reason, sample cleaning is performed prior to every measurement utilizing the output of a 172-nm excimer xenon lamp in a 1%  $\text{O}_2$  ambient. We find that for bare substrates, 15–20-min irradiation is sufficient to induce full recovery of the transmission of a sample that had been exposed to typical contamination [3]. Figure 3-1 shows the transmission of a freestanding 1- $\mu\text{m}$ -thick organic pellicle material as-received and after 172-nm lamp cleaning. Within the first 15 min of lamp cleaning significant recovery of transmission takes place throughout the uv spectrum. Most pronounced is bleaching of the aromatic absorption around 195 nm, which can be characteristic of surface contamination. The absence of fringe shifts suggests that no thinning of the material has occurred. For a nominal lamp power of  $2 \text{ mW/cm}^2$ , the pellicle received about  $10 \text{ J/cm}^2$  of 172-nm incident irradiation with no signs of degradation. Transmission of the material at 157 nm, averaged over adjacent fringes, shows a steady recovery and a potential saturation around 92%.

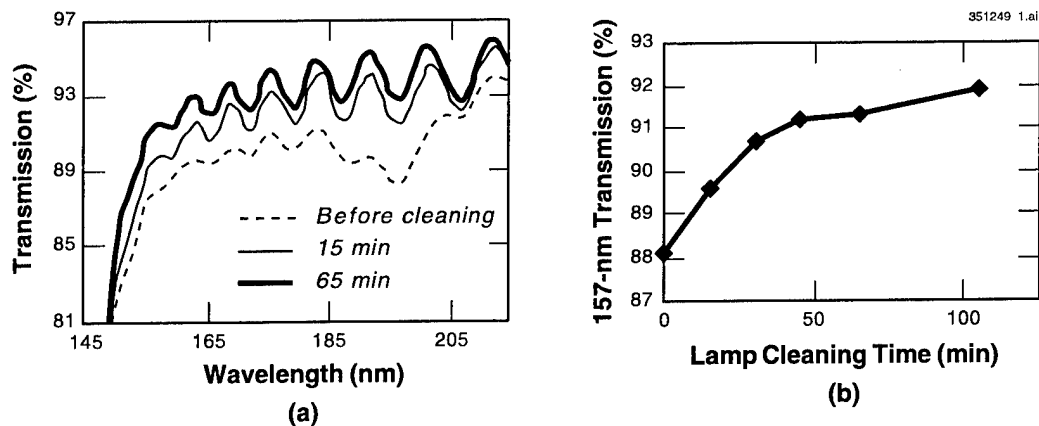


Figure 3-1. (a) Spectral transmission of as-received pellicle material before and after lamp cleaning, and (b) average 157-nm transmission values of the pellicle material as a function of lamp cleaning time.

Irradiation of the same material with 157-nm laser, however, shows a fast decay in transmission over the first few joules of dose, as seen in Figure 3-2. In these experiments the material is irradiated at an incident fluence of  $0.1 \text{ mJ/cm}^2/\text{pulse}$  and a laser repetition rate of 100 Hz in an ambient containing either 1 or 100 ppm of oxygen.

The rapid degradation of material transmission reveals laser-irradiation lifetimes 2–3 orders of magnitude lower than the expected targets. A slight reduction of degradation rate can be seen for the material irradiated under 100 ppm of  $\text{O}_2$ . The transmission trends in Figure 3-2 are typical of most samples tested to date, displaying three distinct regions as a function of incident dose: initial recovery of transmission, a plateau, and a transmission decay.

Up to now we evaluated nearly 100 different pellicle materials, some freestanding membranes, others spun-cast on transparent substrates. While the degradation rates shown in Figure 3-2 are typical for freestanding samples, variations of up to an order of magnitude in laser-induced degradation have been observed among polymer samples spun cast onto  $\text{CaF}_2$  substrates. The variations may be caused by both the polymer and solvent chemistries. These data are discussed in much greater detail in a separate paper [4].

Upon conclusion of laser irradiation, a sample was transferred into the spectrometer chamber, where spectral transmission was obtained before and after 172-nm lamp cleaning. Figure 3-3(a) shows a sequence of transmission scans taken prior to lamp cleaning and after 20 and 40 min, respectively. The fringe-averaged laser-induced losses, shown in Figure 3-3(b), are obtained by referencing the above transmission scans to those obtained prior to irradiation but after 105 min of cleaning, as seen in Figure 3-1(b). The



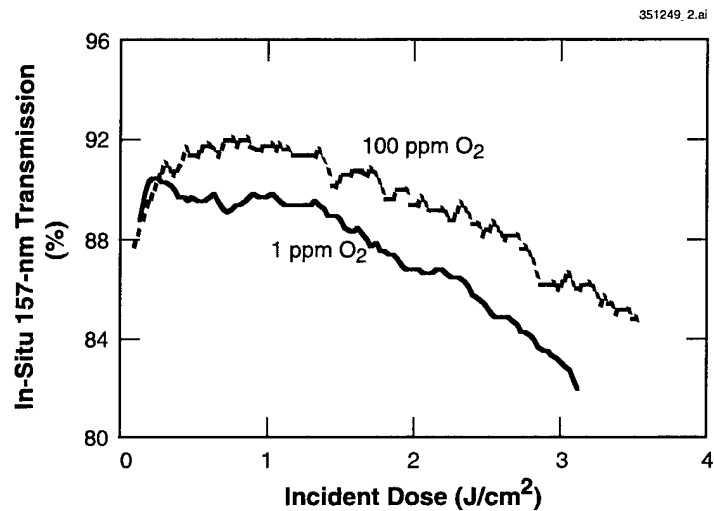


Figure 3-2. Laser-based testing of two freestanding pellicles under 1 and 100 ppm O<sub>2</sub>, respectively.

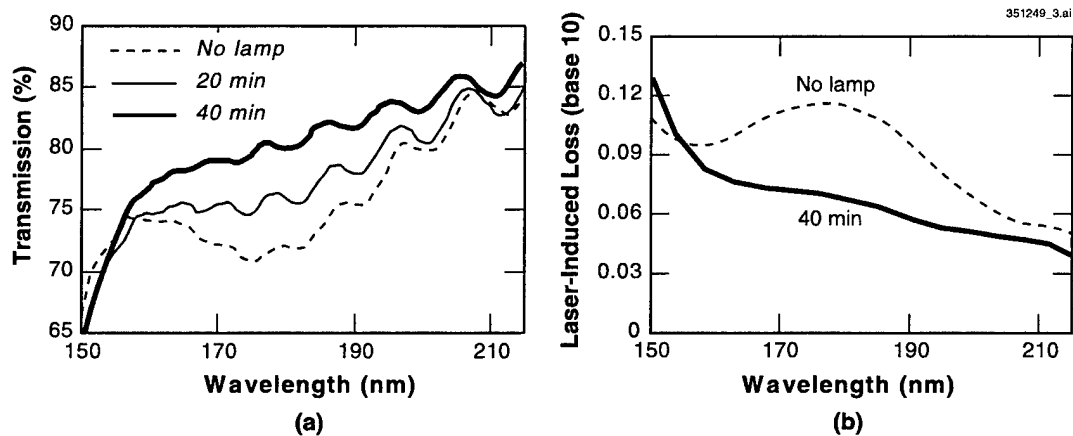


Figure 3-3. (a) Transmission of laser-irradiated freestanding pellicle material immediately after irradiation and after lamp-based cleaning. (b) Comparisons of laser-induced losses prior to and after lamp cleaning.

main effect of lamp cleaning appears to be removal of an absorption band centered at 175 nm. On the other hand, the 157-nm transmission does not exhibit significant recovery after lamp cleaning. Since laser-damaged pellicles absorb a significant amount of lamp irradiation, both thermal effects and photobleaching could be responsible for removal of the 175-nm band. More materials testing in the near future is expected to elucidate laser-induced damage mechanisms in greater detail as a function of pellicle composition and under different testing conditions.

V. Liberman	M. Rothschild
N. N. Efremow	S. T. Palmacci
J. H. C. Sedlacek	C. Van Peski*
K. Orvek*	

### 3.2 HIGH-RESOLUTION FLUOROCARBON BASED RESIST FOR 157-nm LITHOGRAPHY

Lithography at 157-nm wavelength represents the next evolutionary step in optical lithography and is clearly seen as the likely successor to 193-nm lithography. If successful, the photoresists used for this technology must be initially capable of 100-nm resolution and be extendable to less than 70 nm. As with the transition to shorter wavelengths in the past, the photoresist materials developed for longer wavelengths appear to be too absorbent for practical use as a traditional high-resolution single-layer resist imageable with 157-nm radiation. The high 157-nm absorbance of conventional polyacrylate, polycyclic, and polyhydroxystyrene copolymer resists will force the coated resist thickness to be under 100 nm.

It has been shown that some fluorine-functionalized polymers are more transparent in this spectral region than pure hydrocarbon polymers. This has led us to investigate the use of fluorocarbon polymers in resists specially designed for 157-nm lithography. We have synthesized and evaluated a number of unique 4-hexafluoroisopropanol styrene based polymer systems that yield resists in which the 157-nm absorbance ranges from 3.0 to 4.0  $\mu\text{m}^{-1}$ . Resists of this type are potentially capable of imaging at resist thickness of 150 nm.

Copolymers and terpolymers of 4-hexafluoroisopropanol styrene have been prepared that are analogs to the hydroxystyrene-co-t-butyl acrylate polymers. A variety of different monomers can be copolymerized with 4-hexafluoroisopropanol styrene to lead to a number of fluorine-containing copolymers and terpolymers. The 157-nm absorbance of these polymers has been extensively studied and found to range between 3.0 and 4.0  $\mu\text{m}^{-1}$  at 157 nm [5]. The 157-nm absorbance for the polymers along with their glass transition temperatures are presented in Table 3-1.

This hexafluoroisopropanol styrene (HFIP-styrene) platform offers the ability to tailor lithographic performance from a relatively simple synthetic scheme while building on the knowledge base developed

---

\*Author not at Lincoln Laboratory.

**TABLE 3-1**  
**Comparison of Hydroxystyrene Polymer with Several Hexafluoroisopropanol**  
**Styrene Polymers All Containing a 60:40 Copolymer Ratio**

Polymer	$\alpha_{157} (\mu\text{m}^{-1})$	$T_g (^\circ\text{C})$
Poly(4-hydroxystyrene-co-t-butyl acrylate)	6.5	155
Poly(4-HFIP-styrene-co- t-butyl acrylate)	3.7	120
Poly(4-HFIP-styrene-co-t-butyl methacrylate)	4.0	154
Poly(3-HFIP-styrene-co-t-butyl methacrylate)	3.9	111

for the hydroxystyrene platform. Absorbance of the HFIP-styrene platform is such that 100–150-nm thicknesses are possible, thicknesses that when used with a hard mask could enable the early introduction of 157-nm lithography into device manufacturing and effectively negate the need for heavily fluorinated resins that maximize transparency at the expense of manufacturing cost and development effort.

A critical assumption in pursuing the HFIP-styrene approach toward the development of 157-nm resists is the ability of these resists to show imaging characteristics appropriate to sub-100-nm lithography at resist thicknesses of 100 nm or greater. We have evaluated experimental resists comprising both poly(4-HFIP-styrene-co-t-butyl acrylate) and poly(4-HFIP-styrene-co-t-butyl methacrylate). In addition, the terpolymer, poly(4-HFIP-styrene-co-t-butyl acrylate-co-3,5-di-trifluoromethylstyrene), was also evaluated as a 157-nm sensitive resist.

Projection lithography at 157 nm was performed with a laboratory class projection system based on a Schwartzschild lens (numerical aperture 0.50) with aberration-limited performance. All resists were also evaluated on a mask design that contained a dense line pattern with 150, 180, 200, and 250 nm. Although this system is limited in its ability to provide sub-100-nm imaging, it is very useful for determining preliminary imaging characteristics of the resists. Interference lithography was performed on HMDS treated 4-in. silicon wafers. This interference lithography system gives a very sharp aerial image, with resolution capability of 40-nm lines with a 100-nm pitch demonstrated with a 55-nm-thick hydroxystyrene type resist. This system was used to probe the ultimate optical resolution of the HFIP-styrene based resists.

All copolymer based HFIP-styrene exhibited 180-nm imaging capability on our 157-nm projection system at resist thicknesses of 100 nm. The resist LUVR-20007, employing poly(4-HFIP-styrene-co-t-butyl acrylate), gave 150-nm lines with a 400-nm pitch at 2.8 mJ/cm<sup>2</sup> and LUVR-20026, employing poly(4-HFIP-styrene-co-t-butyl methacrylate), gave 120-nm lines with a 360-nm pitch at 6.5 mJ/cm<sup>2</sup>. Both resists were able to print the 200-nm dense features over several doses and focus fields.

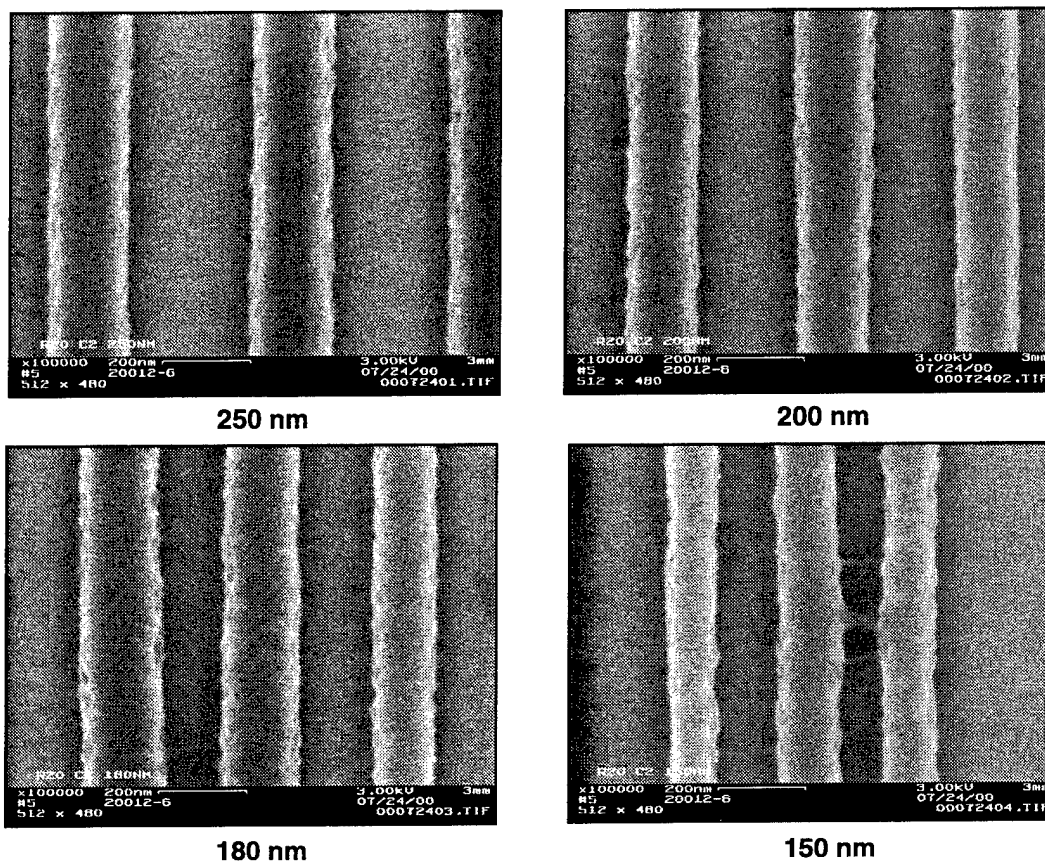


Figure 3-4. Fluorocarbon based 157-nm resist (LUVR-20012) at 100-nm thickness patterned with 250–150-nm features using a 0.50-NA Schwarzschild lens.

An example of the terpolymer imaging at 157 nm for resist LUVR-20012 is presented in Figure 3-4, where all four test features printed, including the nominal 150-nm lines with a 300-nm pitch at 26.9 mJ/cm<sup>2</sup>. This is a very impressive result from this system and matches the best performance observed on this tool, including that previously reported on 60-nm-thick LUVR-99071 resist, which was based on the ESCAP polymer [6]. All three resists capably represented imaging artifacts in that issues attributed to focus, illumination, and vibration were identified, and thus are capable of acting as a tool testing resist.

A final example of the imaging capability at 157 nm of the HFIP-styrene resists from our interference lithography system with LUVR-20007 at 6.5 mJ/cm<sup>2</sup> is seen in Figure 3-5. The resist is capable of imaging 40-nm lines with a 100-nm pitch. Visual comparison of line-edge roughness shows that

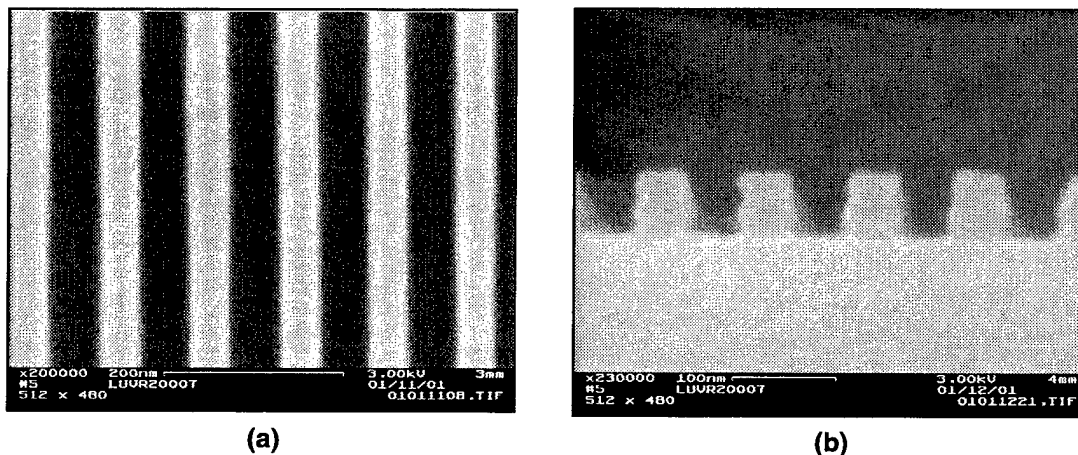


Figure 3-5. Fluorocarbon based 157-nm resist (LUVR-20007) at 100-nm thickness patterned with 40-nm dense lines on a 100-nm pitch using an interference lithography system: (a) top-down view of features and (b) cross-sectional view showing standing waves in the resist sidewalls.

the LUVR-20007 resist gave qualitatively very smooth lines at 40 nm with almost no line-edge roughness. Cross-sectional analysis of the 40-nm lines shows relatively straight resist side walls and flat resist tops. The transparency of the resist at 100-nm resist thicknesses is such that standing waves can be seen in the resist cross section. Measurement of resist thickness before and after development showed no unexposed resist thickness loss, and this is interestingly confirmed by calculating the standing-wave period and noting that at 100-nm resist thickness, three standing wave nodes should be present in a 100-nm-thick resist.

The preliminary resist imaging of the HFIP-styrene polymers is very encouraging. It is noted that these resists are not based on optimized formulations and represent only a first-generation resist system. It can be expected that further work on HFIP-styrene based polymers can lead to improved resist performance. But even so, the imaging capability observed so far, coupled with the relatively straightforward polymer synthesis, makes insertion of this class of resists into the International Technology Roadmap's 95-nm node in 2004 and the 65-nm node in 2007 very possible if coupled with hard mask resist processing technology.

T. H. Fedynyshyn	R. R. Kunz
R. F. Sinta	M. Sworin
W. A. Mowers	R. B. Goodman
S. P. Doran	

## REFERENCES

1. *International Technology Roadmap for Semiconductors* (Semiconductor Industry Association, Austin, Tex., 2000).
2. V. Liberman, R. R. Kunz, M. Rothschild, J. H. C. Sedlacek, R. S. Uttaro, A. Grenville, A. K. Bates, and C. Van Peski, *Proc. SPIE* **3334**, 480 (1998).
3. T. M. Bloomstein, V. Liberman, M. Rothschild, D. E. Hardy, and N. N. Efremow, presented at the 26th Annual International Symposium on Microlithography, Santa Clara, Calif., 25 February–2 March 2001.
4. R. H. French, J. Gordon, D. J. Jones, M. F. Lemon, R. C. Wheland, E. Zhang, F. C. Zumsteg, K. G. Sharp, and W. Qiu, presented at the 26th Annual International Symposium on Microlithography, Santa Clara, Calif., 25 February–2 March 2001.
5. R. R. Kunz, R. F. Sinta, M. Sworin, W. A. Mowers, T. H. Fedynyshyn, V. Liberman, and J. Curtin, *Proc. SPIE* **4345** (2001).
6. T. H. Fedynyshyn, R. R. Kunz, S. P. Doran, R. B. Goodman, M. L. Lind, and J. E. Curtin, *Proc. SPIE* **3999**, 335 (2000).

## 4. BIOSENSOR AND MOLECULAR TECHNOLOGIES

### 4.1 RESPONSE OF B CELLS TO SUPERPARAMAGNETIC PARTICLE SIMULANTS

Increasing awareness of the threat posed by biological weapons underscores the need for devices capable of sensitive, rapid, and reliable detection and identification of bioagent releases. To meet this need, we have been developing a novel bioelectronic sensor for the detection of viral and bacterial pathogens that exploits engineered elements of the natural immune response, as described previously [1]–[4]. The cornerstone of the CANARY (Cellular Analysis and Notification of Antigen Risks and Yields) sensor is a cell line derived from B cells, a type of white blood cell that expresses antibodies on the outer membrane that bind specifically to a particular molecule (antigen). Antibody-antigen interaction generates a chemical signal inside the B cell that undergoes several levels of amplification and causes an increase in the internal calcium-ion concentration. We have engineered (i.e., added genetic material to) an immortal B cell line (atypical B cells that can be cultured outside a living host and replicate by cell division) to express the photoprotein aequorin. This protein, which is normally found in luminescent jellyfish, produces light in response to increases in calcium concentration by oxidizing its cofactor, coelenterazine. The aequorin produced inside the engineered B cell emits light as calcium levels rise following antigen binding. Introduction of additional genetic material causes the B cell to produce and display antibodies on the cell surface that recognize and bind to the desired antigens. In this way, we have developed cells that emit photons following exposure to specific bioagents. Cell lines are currently available for the bacteria causing tularemia (*Francisella tularensis*) and plague (*Yersinia pestis*) and the viral agents causing foot and mouth disease (A strain) and Venezuelan equine encephalitis. Development of B-cell lines specific for six other bioagents and simulants is currently under way.

Previous simulations of cell-particle interactions and investigations of photon output from B cells exposed to decreasing concentrations of particles in test tubes suggested that the rate of diffusion is likely to limit both the speed and sensitivity of many potential CANARY sensor designs. As shown in Figure 4-1, we have developed a simple approach to overcome these diffusion limits by forcing particles together using a centrifuge. Centrifugation increases the peak photon output and reduces the response time for B cells exposed to sedimentable particles. Without centrifugation, photon output from mixing 25,000 B cells with 530,000 tularemia particles produces a maximum photon output of 1000 photons/s after 300 s. Centrifuging a mixture containing the same number of B cells and tularemia particles for 5 s at 13,000 rpm (5600 g's) drives the B cells and a portion of the tularemia particles together at the bottom of the tube and improves the maximum photon output to 3200 photons/s after only 100 s. Signal intensity is further optimized by collecting all of the tularemia particles in the bottom of the tube by centrifuging for 1 min at 5600 g's prior to adding B cells and driving them into the collected particles with a subsequent 5-s spin. By using this centrifugation sequence, photon output peaks at 30,000 photons/s after 150 s (including the initial 60-s spin).

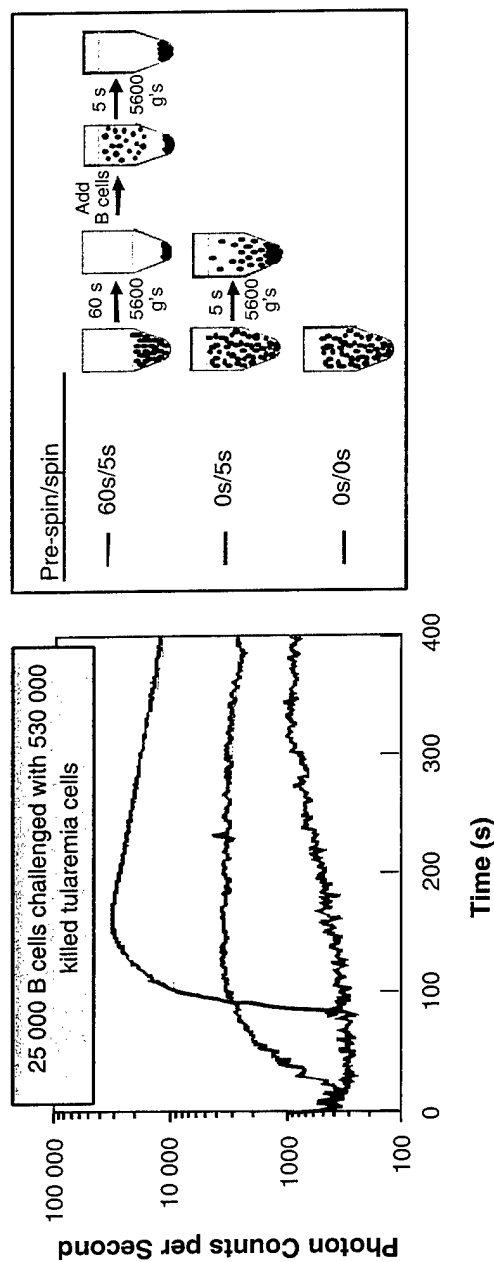


Figure 4-1. Centrifugation enhanced CANARY (Cellular Analysis and Notification of Antigen Risks and Yields) format. Top: Photographs of centrifugation setup in (left) spinning (13,000 rpm) and (right) measuring modes. Bottom: Plot of photon output produced by exposure of 25,000 B cells to 530,000 killed tularemia particles with and without centrifugation enhancement procedures as indicated in the schematic at right, where tularemia particles are represented by black circles and B cells by larger red circles.



The improved signal-to-background characteristics of the centrifuge-assisted CANARY protocol enable identification of bacterial agents at lower concentrations. Typical results for detection of killed tularemia are shown in Figure 4-2. A dose-response overlay plot is presented in Figure 4-2(a), demonstrating the broad dynamic range and sensitivity for CANARY-based detection of tularemia particles. The specificity of the B cell response is also evident from the lack of photon output stimulated by the addition of more than 5 million particles of killed plague-causing bacteria. Using this assay format, we are able to consistently detect as few as 60 tularemia particles in less than 3 min as shown by the representative raw data in the right panel of Figure 4-2. The demonstrated sensitivity of the CANARY assay compares well with that of the most sensitive identification methods based on polymerase chain reaction (PCR) technology, which are capable of detecting and identifying <10 DNA molecules. However, CANARY provides identification in  $\leq 3$  min compared to  $\sim 30$  min for PCR-based assays under ideal conditions. Furthermore, we believe that even lower limits of detection for CANARY may be possible with optimization of light collection, application of signal processing algorithms, and further bioengineering to increase the photon output of the B cells used in the assay.

The functionality of the optimized centrifuge sensor format has been incorporated into a portable prototype shown in Figure 4-3 that was designed and built in-house. The prototype unit is intended for use in technology validation tests to be performed in other laboratories, including testing against live pathogenic agents in BL-3 facilities, and is currently being characterized and validated in side-by-side testing with our original bench-top apparatus.

Further developments in sensor architecture may be particularly important for realizing the full speed and sensitivity of the CANARY technology for slowly sedimenting analytes including protein toxins and small viruses. We have surveyed additional techniques with the potential to rapidly focus analytes and subsequently promote their interaction with B cells. Based on our findings, we are investigating the utility and compatibility of membrane filtration, affinity capture, and electrophoretic manipulation strategies.

J. D. Harper	R.H. Mathews
F. E. Nargi	M. S. Petrovick
T. H. Rider	M. A. Hollis
J. Chen	

## REFERENCES

1. Solid State Research Report, Lincoln Laboratory, MIT, 1998:4, p. 27.
2. Solid State Research Report, Lincoln Laboratory, MIT, 1999:1, p. 21.
3. Solid State Research Report, Lincoln Laboratory, MIT, 1999:2, p. 21.
4. Solid State Research Report, Lincoln Laboratory, MIT, 2000:4, p. 29.

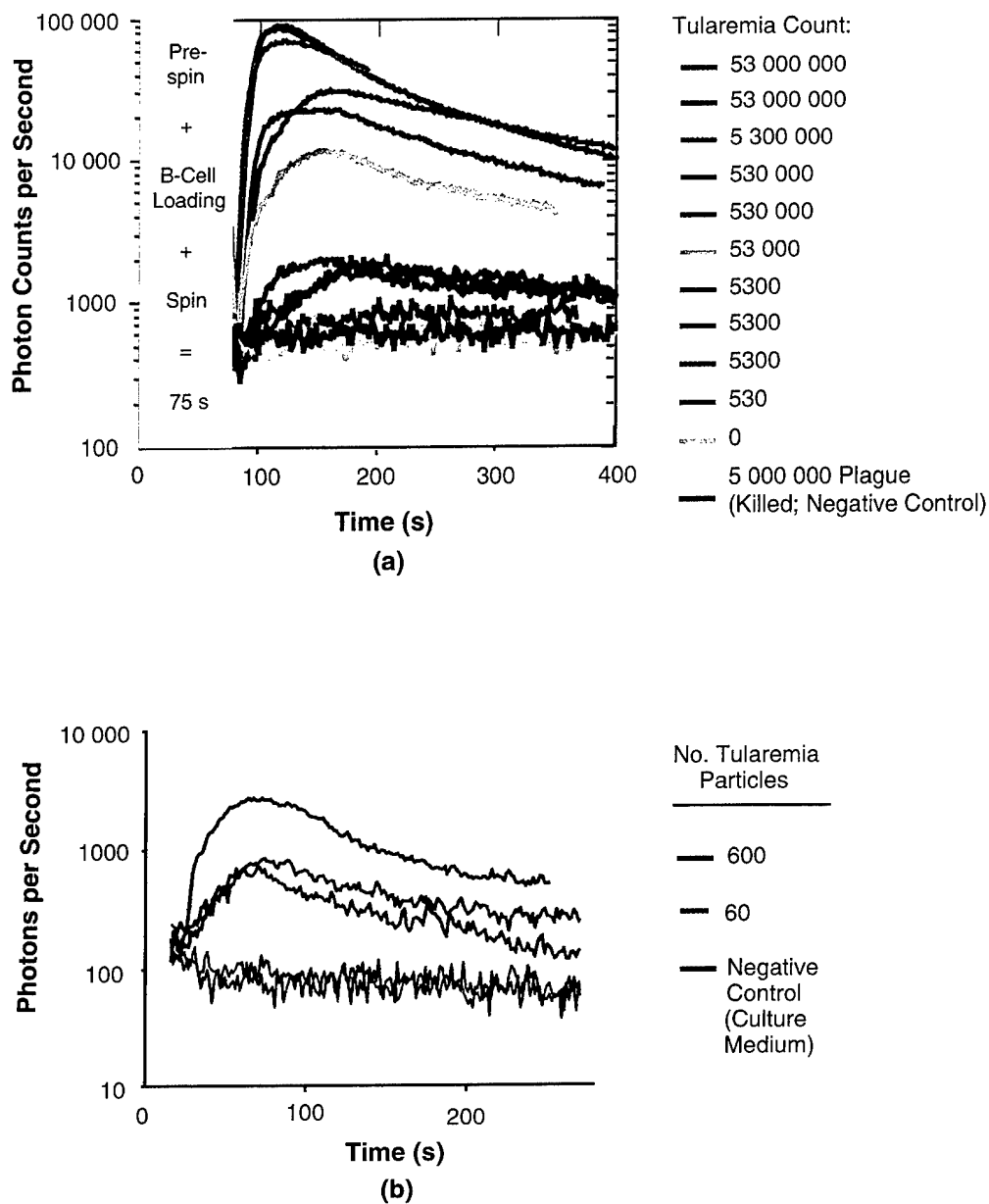
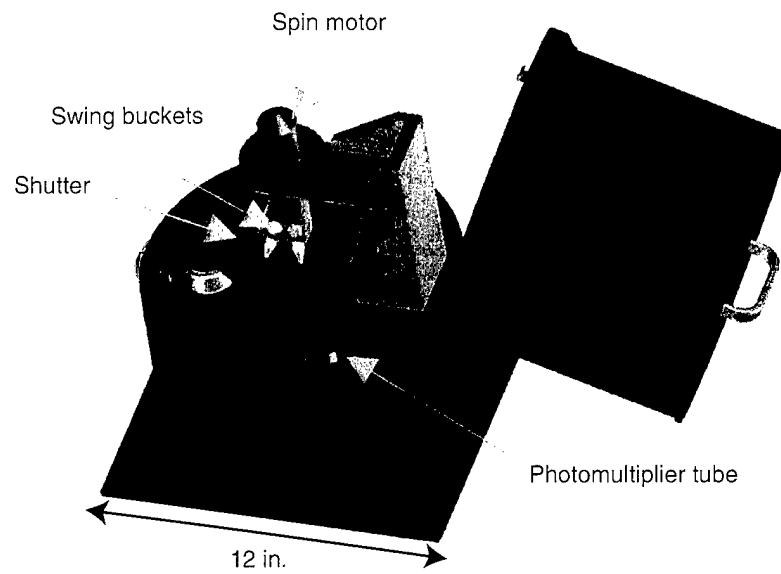


Figure 4-2. Detection of killed tularemia by CANARY B cells: (a) dose response for B cells exposed to the numbers of tularemia particles and control samples indicated, showing the broad dynamic range and extreme specificity of this identification sensor technology, and (b) typical unfiltered data demonstrating excellent signal-to-background ratios for identification of 60 tularemia particles.



*Figure 4-3. Design and dimensions of the portable CANARY microcentrifuge sensor prototype built for live agent testing and other collaborative development work requiring a portable sensor unit.*

## 5. ADVANCED IMAGING TECHNOLOGY

### 5.1 BACK ILLUMINATION OF LARGE-AREA CCD IMAGERS USING MOLECULAR BEAM EPITAXY

In conventional operation, a charge-coupled device (CCD) is illuminated through the side of the device where the polysilicon clocking gates have been deposited. This leads to simplified processing, but it also decreases the quantum efficiency of the device, since significant amounts of blue, uv, and low-energy x-ray photons are absorbed in the polysilicon. To avoid this problem, various techniques have been employed for back illumination of the CCD [1],[2]. For this type of processing to be successful, the back surface must be treated, which includes creating a large boron doping gradient to decrease the recombination of photogenerated carriers and to drive photoelectrons through the neutral and depleted regions of the CCD, towards the *n*-Si buried channel. Typically, the back-illuminated CCD is only some tens of micrometers thick, to limit lateral diffusion of the electrons.

Recently, another back-surface treatment has been developed using molecular beam epitaxy (MBE) to provide the thin *p*-doped layer, and has been applied to a large-area CCD imager developed for astronomy [3]. This technique is quite similar to that used previously [4]. In particular, the central disk of a 150-mm-diam wafer is thinned to thickness of about 45  $\mu\text{m}$ , leaving a supporting rim only 2–3 mm wide around the perimeter. The entire wafer, with the front side metallization intact, is then subjected to standard semiconductor cleans in sulfuric acid–hydrogen peroxide, amine alcohol, and hydrofluoric acid solutions and inserted in the MBE apparatus. After the heating and desorption of adsorbed layers from the wafer, a degenerately doped *p*-Si layer, several nanometers thick, is deposited on the back side of the wafer. This deposition occurs at a temperature of about 400°C, so the metallization is not affected. In-situ reflectance high-energy electron diffraction reconstruction patterns indicate the quality of the deposited layer is very good. Studies are under way to examine the bulk-epitaxial interface using transmission electron microscopy.

After the MBE deposition the thinned wafer is mounted front side down using epoxy to a carrier wafer, to provide mechanical support for the individual chips after they are subsequently sawn apart. Prior to mounting on the carrier wafer, the CCD wafer is coated with a few micrometers of  $\text{SiO}_2$ , either before MBE or afterwards. The back side is coated with a one- or two-layer antireflection coating, and openings are etched through the thin membrane to expose the aluminum bond pads on the front side of the devices. At this point, the wafer is sawn up and individual devices are wire bonded, allowing for test of the operating characteristics, including the quantum efficiency (QE) of the device between 200 and 1000 nm.

In general, the performance of the devices is comparable to that of devices processed by the ion-implant/laser anneal process, with the exception of the improved QE and charge-transfer efficiency which has not yet been evaluated. Perhaps the most remarkable characteristic is the QE, as seen in Figure 5-1. The two measured curves are for a bare Si device and a coating of  $\text{HfO}_2$ , optimized for transmission

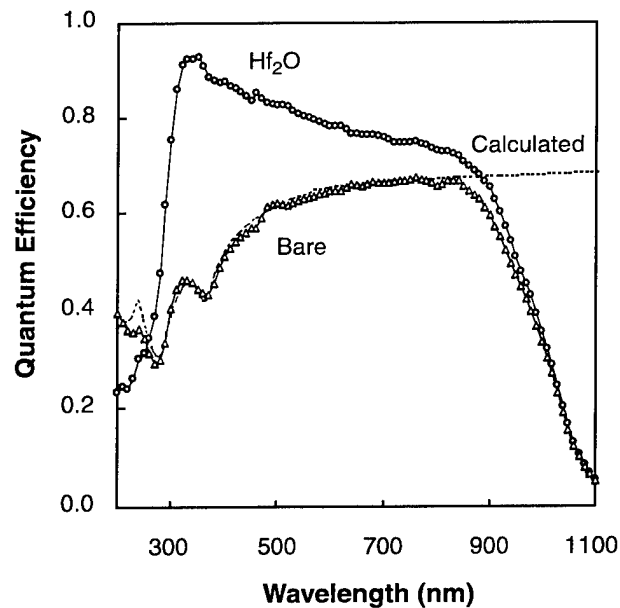


Figure 5-1. Quantum efficiency of back-side-illuminated CCD in the visible and near visible.

around 320 nm. The dashed curve indicates the calculated value of a bare device with a 100% internal QE, i.e., disregarding reflection losses. Note this curve lies on the bare Si data within experimental accuracy, except for the range between 210 and 250 nm (this deviation may be due to the presence of a contaminating organic layer). Above 850 nm, the QE falls because the absorption length in Si exceeds the device thickness. Between 200 and 400 nm, on the other hand, the absorption distance is on the order of 3–5 nm thick, indicating the MBE layer acts superbly as a passivant for the illuminated back side. The HfO<sub>2</sub>-coated curve also indicates an external QE above 90% in the optimal wavelength region, where the absorption distance is quite short and other passivation techniques yield QE between 20 and 30% [2]. It is expected the QE will be high for low-energy x-rays ( $E < 1000$  eV), where the absorption distance in Si is again quite small.

In summary, MBE has extended the useful wavelength range of CCDs (processed at the whole-wafer scale) to the near uv where the absorption distance is only a few nm.

S. D. Calawa	A. H. Loomis
P. M. Nitishin	T. A. Lind
J. A. Gregory	B. E. Burke

## REFERENCES

1. C. M. Huang, B. B. Kosicki, J. R. Theriault, J. A. Gregory, B. E. Burke, B. W. Johnson, and E. T. Hurley, *Proc. SPIE* **14478**, 156 (1991).
2. Solid State Research Report, Lincoln Laboratory, MIT, 1993:1, p. 53.
3. B. E. Burke, J. A. Gregory, A. H. Loomis, C. C. Cook, D. J. Young, M. J. Cooper, T. A. Lind, G. A. Luppino, and J. L. Tonry, *Optical Detectors for Astronomy II*, P. Amico and J. Beletic, eds. (Kluwer, Norwell, Mass., 2000), pp. 187-199.
4. S. Nikzad, M. E. Hoenk, P. J. Grunthaner, R. W. Terhune, F. J. Grunthaner, R. Wizenread, M. Fattahi, and H.-F. Tseng, *Proc. SPIE* **2278**, 138 (1994).

## 6. ANALOG DEVICE TECHNOLOGY

### 6.1 CORRELATION PROCESSOR CHIP FOR NOISE-CORRELATION RADAR

A processor chip has been developed for an advanced noise-correlation radar (NCR) application [1]. Instead of transmitting carefully crafted waveforms, such as pseudonoise sequences or chirps, this radar uses true random noise as its modulation source. Because the processing gain possible with random noise signals is limited, coherent processing over a large number of code “chips” is required. To achieve this, the radar must operate with a very high bandwidth and a high duty cycle.

The front-end signal processing for such a radar involves the following steps:

1. Information about each transmitted pulse is stored
2. Information about each return signal is correlated against the information about the corresponding transmitted signal over a span of target ranges (range bins)
3. The correlation values for each pulse are stored in a so-called corner-turning memory
4. The steps above are repeated over a time interval known as the coherent processing interval (CPI)
5. The correlation values are then read out from the corner-turning memory in a different order—data from all transmitted pulses for each range bin—and sent to a fast Fourier transform (FFT) chip to form a Doppler (velocity) map

One component of the overall NCR program called for the development of chips for a real-time processor with the goal of showing that the required signal processing can be performed in real time within power-consumption and size constraints appropriate for a compact missile seeker. We describe here the correlation processor chip (“correlator chip” for short) that performs the first two signal-processing steps above.

Figure 6-1 shows a cartoon scenario illustrating the operating mode of an NCR in a missile seeker. A cueing radar of conventional design, here shown in an aircraft, determines the approximate position and velocity of the target relative to the seeker. That information is transmitted to the seeker, where it is used in determining the operating configuration of the NCR. The radar operates with the following nominal characteristics:

1. The pulse repetition interval (PRI) is  $1\ \mu\text{s}$ , corresponding to a spatial separation between pulses of 300 m
2. The transmitted and received signals are sampled at a 1-GHz rate

3. In-phase (I) and quadrature (Q) samples are captured with a resolution of 1 bit (the sign of the signal), thereby specifying the quadrant into which the phase of the signal falls but providing no amplitude information
4. In-phase and quadrature correlation terms are computed, producing a correlation vector with amplitude and phase
5. For the transmitted reference, 112 chips ( $0.112 \mu\text{s}$ ) are sampled and stored, and the raw correlation terms range between  $-56$  and  $+56$ .
6. For the return signal, 368 chips are sampled and stored, allowing 256 range bins to be processed ( $112 + 256 = 368$ ), and the 1-ns time between samples corresponds to a target range-bin size of 15 cm (6 in.) and a total range coverage of 38.4 m (128 ft).

The very high pulse repetition frequency (PRF) gives rise to an unusual situation: many transmitted pulses are typically in space at the same time, as shown in Figure 6-1. This requires that multiple reference patterns be saved and that each return signal be correlated against its corresponding transmitted reference pattern. The correlator chip stores up to 32 reference patterns, sufficient for a maximum range at a  $1\text{-}\mu\text{s}$  PRI of  $32 \times 300 \text{ m} \div 2 = 4.8 \text{ km}$ . The chip's internal timing circuitry can handle ranges up to twice that distance for longer PRI values.

In order to prevent return signals from arriving during the time when another pulse is being transmitted, the PRI must be varied from CPI to CPI depending on the target range interval to be covered. The chip supports PRI values from less than  $0.5 \mu\text{s}$  to more than  $4 \mu\text{s}$ . To allow flexibility in the length of the transmitted signal, the correlator chip can handle shorter code lengths of 64, 80, and 96 in addition to the nominal value of 112.

The CPI for the radar is nominally 10 ms, limited by the time interval over which the target can be treated as having a constant velocity and by the maximum allowable delay in the control loop for missile guidance. For a PRI of  $1 \mu\text{s}$ , the CPI thus comprises approximately 10,000 pulses. Generating the range-Doppler maps requires 256 FFTs to be carried out in 10 ms, or  $40 \mu\text{s}$  per transform. To ease the stress on the FFT chip and to reduce the data rate from the correlator chip, several correlation results (nominally 5) are combined ("presummed") on the chip. This allows correlation results to be read out from the correlator chip over  $5 \mu\text{s}$  instead of  $1 \mu\text{s}$ , and the FFT only has to perform 2048-point transforms instead of 10,000-point transforms. The correlator chip supports presum values from 1 (no presumming) to 16.

Successive correlation terms cannot be presummed simply by adding them, because significant phase shifts can occur from one radar pulse to the next. Consequently, the correlator chip must perform vector rotations on the individual correlation terms to bring them into approximate phase alignment before they are summed. For flexibility, instead of computing the rotation terms on the chip, parameters WINCOS and WINSIN representing weighted ("windowed") cosine and sine values are loaded onto the chip and



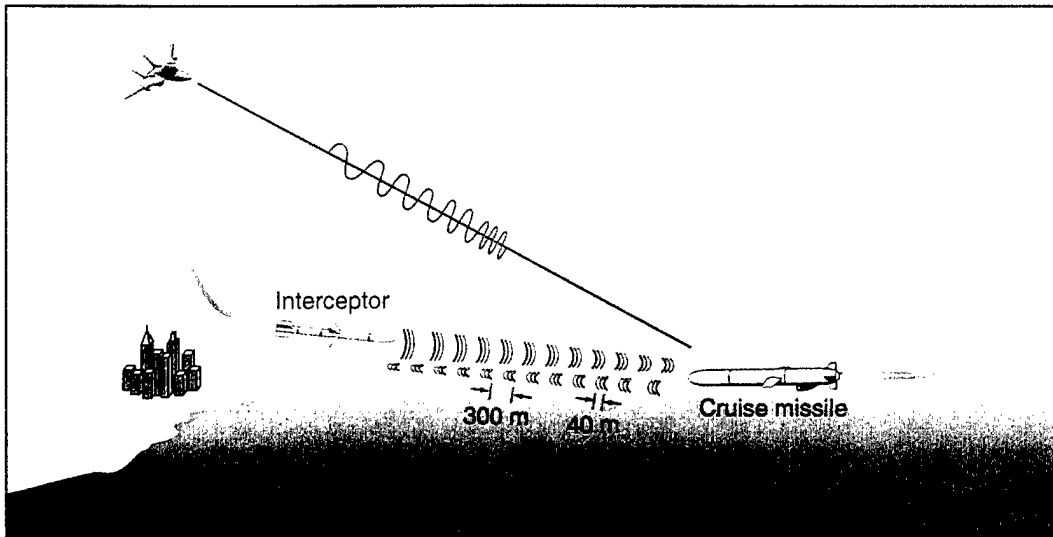


*Figure 6-1. Scenario in which a noise-correlation radar might be used, illustrating some of its unusual characteristics, such as the very high pulse repetition frequency that results in multiple transmitted pulses in space at any given time.*

stored with each packet of reference data. After the return signal has been captured and correlated against its reference, WINCOS and WINSIN are used to rotate the phase and to apply any windowing function needed to suppress artifacts in the later FFT computation.

The correlator chip performs one other very important function. Even for moderate target velocities relative to the radar, a target will not remain in the same absolute range bin during an entire CPI; for high velocities, the target may drift across nearly the entire 256-range-bin interval. In the absence of corrective action, the range-Doppler map will be blurred, and the peak signal amplitude greatly reduced. To avoid this, the correlator chip was designed to shift the entire range interval at a rate corresponding to a nominal target velocity loaded into a register on the chip. If the nominal velocity is close enough to the actual target velocity, the returns over the entire CPI can be maintained in a single range bin.

The architecture of the correlator chip is shown in Figure 6-2. The chip contains three sections that operate at different frequencies. One of the design strategies was to minimize the amount of circuitry that must run at the full data rate of the radar and to do as much of the data processing as possible at lower frequencies. The section at the left, shown in red, operates at the radar clock rate (nominally 1 GHz) and performs two kinds of functions: it performs the timing functions required to determine when input data should be captured, and it captures the input data. The first of these functions is the most complex, involving a number of presettable counters.

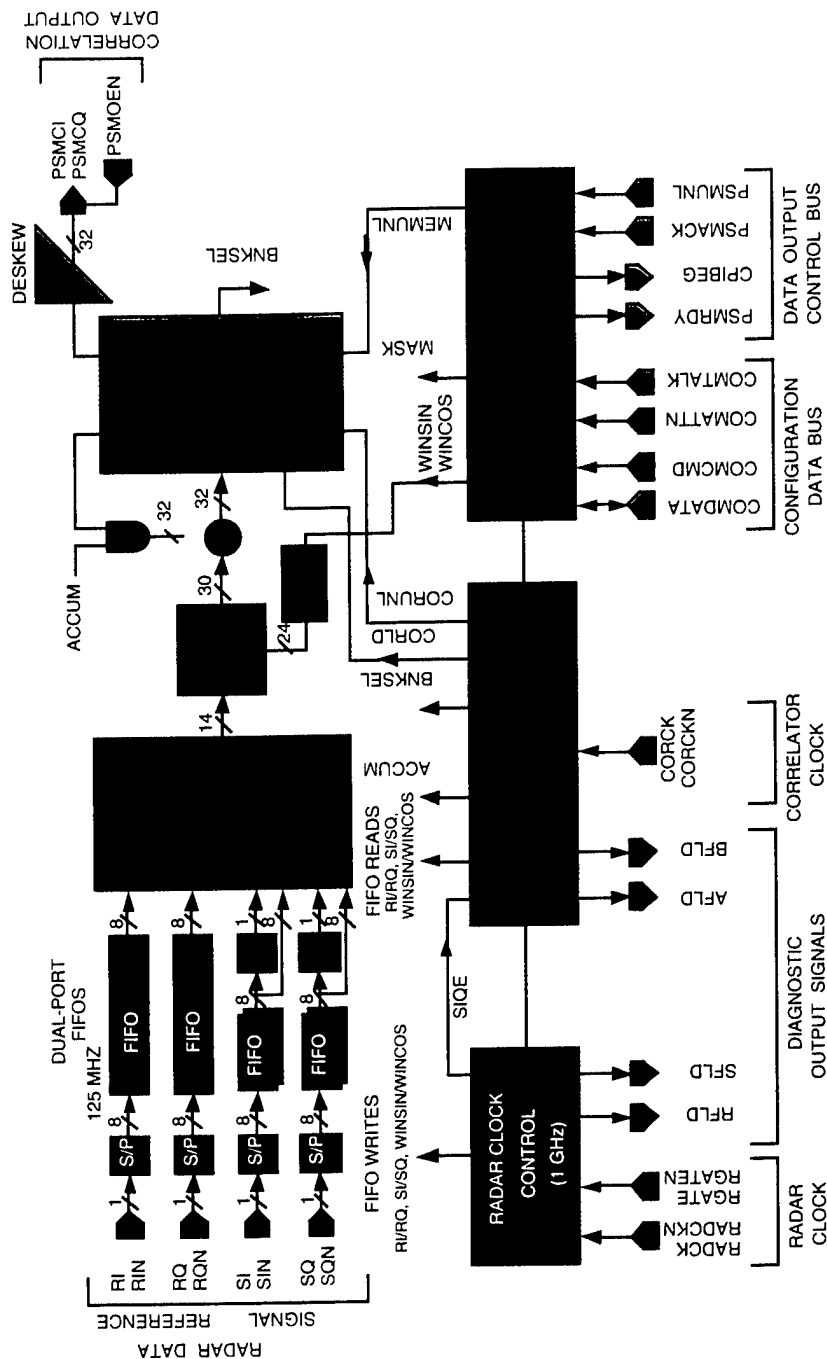


Figure 6-2. Block diagram of real-time correlation processor chip. The red section operates at the full radar clock frequency of 1 GHz, capturing and storing reference and signal data from the radar at times that it computes based on radar operating parameters written to the chip. The green section processes the data at a lower, "correlator" clock frequency of 280 MHz. The blue section, which can operate at 55 MHz, provides communication with the rest of the signal processing system.

The input radar data comprises in-phase and quadrature reference data (RI, RQ) and in-phase and quadrature return signal data (SI, SQ), all at the rate of the radar clock (RADCK). A “radar gate” (RGATE) signal indicates by its rising edge that a new transmitted pulse and burst of RI/RQ data have begun. In fact, the chip requires the RGATE signal only for the first transmission of a new CPI. After that, the chip maintains internally the timing for the entire CPI, during which it ignores the RGATE signal. The correlator is primed for a new CPI by a parameter written via its configuration bus, described later.

During an entire CPI, the chip times when RI/RQ signals need to be stored and when SI/SQ signals need to be stored, taking into account programmed values for the PRI, target range, and target speed (range-walk rate). Across the boundary between successive CPIs, the control logic actually keeps track of RI/RQ timing based on the characteristics of the new CPI while continuing to capture and process SI/SQ data based on the characteristics of the old CPI until the first return pulses for the new CPI begin to arrive back at the radar.

Input data are captured into 8-bit-long shift registers and transferred out in parallel as bytes at one-eighth the rate (125 MHz) into dual-ported static random-access memory (SRAM) modules that act as first-in–first-out (FIFO) buffers. The reference FIFO has the capacity to store 32 sets of reference data. Two banks of signal FIFO are provided so that signal data can be read out from one bank over an entire PRI while new data are being written to the other bank. Two diagnostic outputs allow one to observe when data are being written into the reference FIFO (signal RFLD) and into one bank of the signal FIFO (signal SFLD).

The processing of the data is performed at the slower “correlator clock” (CORCK) rate by the section of the chip shown in green. Once a new burst of signal data (SI/SQ) has been saved in memory, the 112 bits of the corresponding reference data and the first 112 bits of signal data are read out as a sequence of 14 8-bit blocks and preloaded into the registers in the transversal correlator engine. Then the remaining signal data are clocked through the correlator engine serially until 256 range bins have been processed. This accounts for approximately 270 (14 + 256) clock cycles. To be conservative and to allow for some additional pipeline delays, the correlator clock is specified to be 280 MHz.

As the in-phase and quadrature correlation terms (CI, CQ) emerge from the correlator engine, they undergo phase rotation and scaling in the phase-shifter block. The resulting terms are then added to any previously accumulated presum and stored into one of two banks of presum SRAM. Two diagnostic outputs allow one to observe when data are being written into presum memory banks A (signal AFLD) and B (signal BFLD).

Once a presum has been completed, the presum memory banks are swapped, and the next presum data set is accumulated in the other bank while the previous bank is read out from the chip. Beginning with the summations in the correlator engine, all arithmetic operations and the storage of data in memory are performed in pipeline fashion, with the least significant bit handled first and each successive bit delayed by one clock cycle. The pipeline skew in the stored data is removed only at the output from the chip.

The remaining section of the correlator chip, shown in blue, runs at a relatively slow clock rate, up to 55 MHz. It includes two subsections. One manages the configuration bus; the other manages the readout of correlation data from the chip. The configuration bus is used to load values of the chip's operating parameters and, for diagnostic purposes, also to read back those values. The 12-bit COMDATA bus carries the values; the 4-bit COMCMD bus selects the parameter; COMATTN serves as a write strobe to store a parameter value in the chip; and COMTALK serves as a read strobe, commanding the chip to drive the COMDATA bus.

The parameters that control the chip are listed and described in Table 6-1. Most of them apply for an entire CPI. The most recently written value becomes active at the beginning of a CPI and does not change until the next CPI starts. As noted earlier, however, at the boundary between CPIs, the processing of

**TABLE 6-1**  
**List of All Parameters Whose Values Are Loaded into Correlator Chip**  
**to Control Its Normal Operation**

WINCOS, WINSIN	Cosine and sine values for correcting the phase of each return signal for the Doppler shift expected for the nominal target velocity, multiplied by an apodization window weight for the FFT processing.
NP	The length of the PRI in units of the RADCK period.
NRH, NRL	The high and low parts of a 24-bit word, NR, representing the return delay R of the first transmitted pulse of a CPI in units of the RADCK period. The word NR equals $R \cdot 2^8$ so that the low 8 bits represent a fractional number of RADCK periods.
W	A signed, 2's-complement value that represents the amount by which the return delay changes from one return to the next owing to the nominal target velocity.
L	The code length (number of bits of transmit data). Only bits (6:0) of L will be stored, and only bits 5 and 4 will be used. Bit 6 will be treated as 1 and all others as 0, thereby allowing only values of 64 (00), 80 (01), 96 (10), and 112 (11).
PS	The presum count. Only bits (3:0) will be stored.
CPINew	Primes the correlator to begin a new CPI and optionally resets the data input FIFOs.

reference signals uses the parameters for the new CPI immediately, while the processing of radar return signals continues to use the parameters for the old CPI until the first return of the new CPI comes back. The parameters WINCOS and WINSIN apply only to a PRI, and the most recently written values are stored into a FIFO at the start of each new reference data set. The parameter CPINew is a special case. The act of writing to its address, regardless of the value written, primes the chip to monitor RGATE for the beginning of a new CPI.

The presum data output subsection manages the final processed data. The radar knows when it transmits pulses, but it is a complex task to determine when a set of processed data is ready to be read out of the correlator chip. There is a delay due to the target range (possibly modified by range walk), the pipelined correlation processing, and the accumulation of a presum. Therefore, the chip was designed to provide two output timing signals to the system controller. PSMRDY indicates when a new set of presum data is available. When the PSMRDY strobe appears, the controller must latch the first output data word into a corner-turning memory, pulse the PSMUNL line to advance to the next output word, and repeat that process until all 256 output words have been stored. CPIBEG is asserted along with PSMRDY when the current presum data set is the first one of a new CPI. This signal tells the system controller to swap banks in the corner-turning memory and begin FFT processing on the just-completed CPI.

Figure 6-3 shows the layout of the chip. It is 5 mm on a side and was fabricated through MOSIS by Taiwan Semiconductor Manufacturing Company (TSMC) using their 0.25- $\mu\text{m}$  process. Chips have been packaged and mounted on a high-speed test board. All functions work as designed. In particular, the timing functions have been examined in detail to make sure that the chip responds precisely to the programmed PRI interval, target distance, range-walk rate, and presum setting. The timing circuits all operate up to the design specification of 1 GHz for RADCK and 280 MHz for CORCK.

Figure 6-4 shows the timing of the capture of reference and signal data. The clocks were operating at full speed. The PRI parameter NP was set to 1024 for a PRI of 1.024  $\mu\text{s}$ . The target range parameters NRH and NRL were set to 16 and 0, respectively, corresponding to a range of 256 RADCK cycles. One can see that the timing of the old CPI for reference data capture was terminated immediately on the rising edge of the RGATE signal. In this case the target range is less than the PRI, so the capture of signal data also adjusts immediately to the timing of the new CPI. Note that the SFLD signal shows the capture of data in only one of the two signal FIFOs, and that is why one sees a pulse for only every other pulse in the RFLD signal.

Figure 6-5 shows the timing of the storage of correlation data in the presum memory with the same settings as in Figure 6-4 and the presum parameter PS set to 5. Scaled, rotated correlation data are stored in memory bank A for the first five PRIs; outputs for the next five PRIs go into bank B. As in Figure 6-4, one can see the premature termination of processing data from the previous CPI.

Figure 6-6 shows output from the chip with RADCK reduced to 800 MHz. For reasons we do not yet understand, complete end-to-end signal processing could not be achieved at the full 1 GHz. For this figure, the reference and signal patterns RI and SI were each a square wave with 128 0's and 128 1's, while the

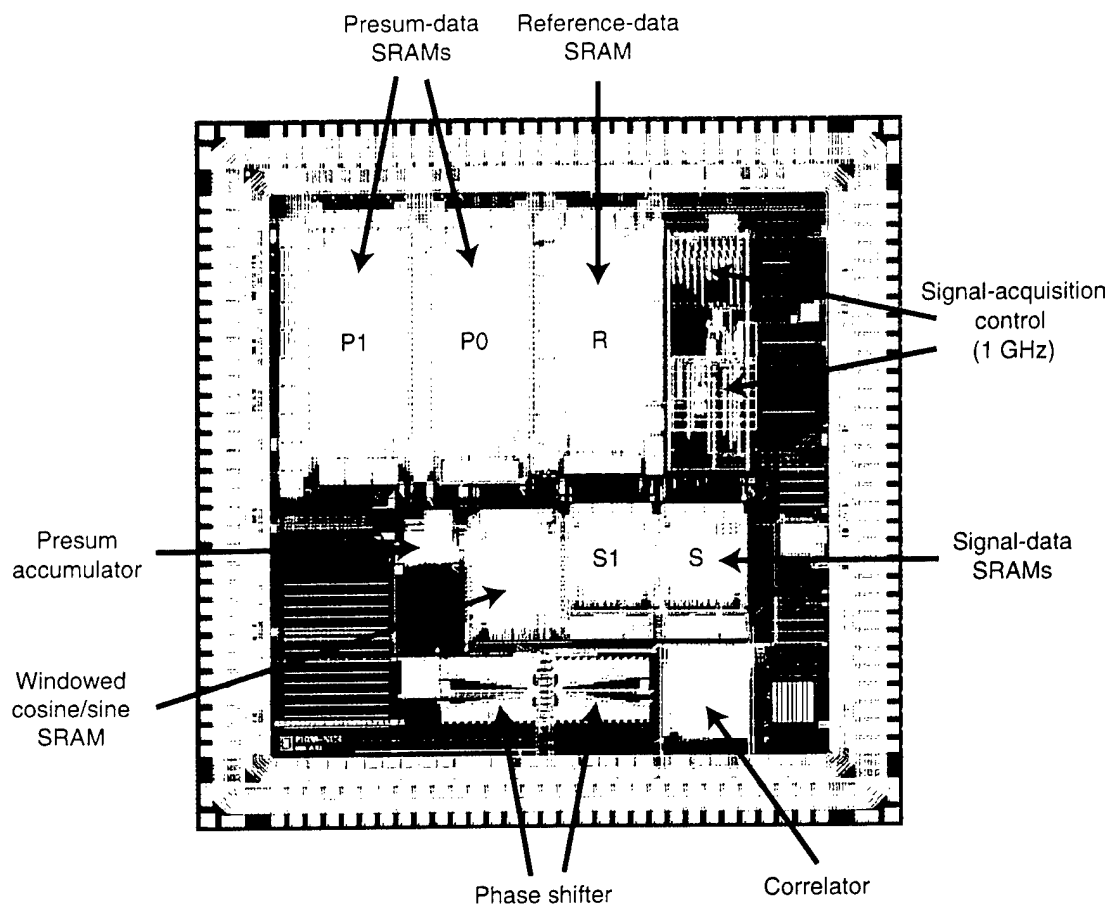


Figure 6-3. Image of the chip layout. The chip is 5 mm on a side.

quadrature inputs RQ and SQ were tied to a 0 level. The timing was adjusted so that the 112-bit RI data set sampled a part of the square wave containing 72 0's and 40 1's. The input data patterns and the parameters controlling code length, weighted cosine and sine, and presum count were varied extensively, and in all cases the output correlation values agreed exactly with the values calculated mathematically.

J. Sage                      R. Berger  
D. Santiago                M. Seaver

## REFERENCE

1. "Pentagon seeks new anti-missile concepts," *Aviat. Week Space Technol.*, 25 September 2000.

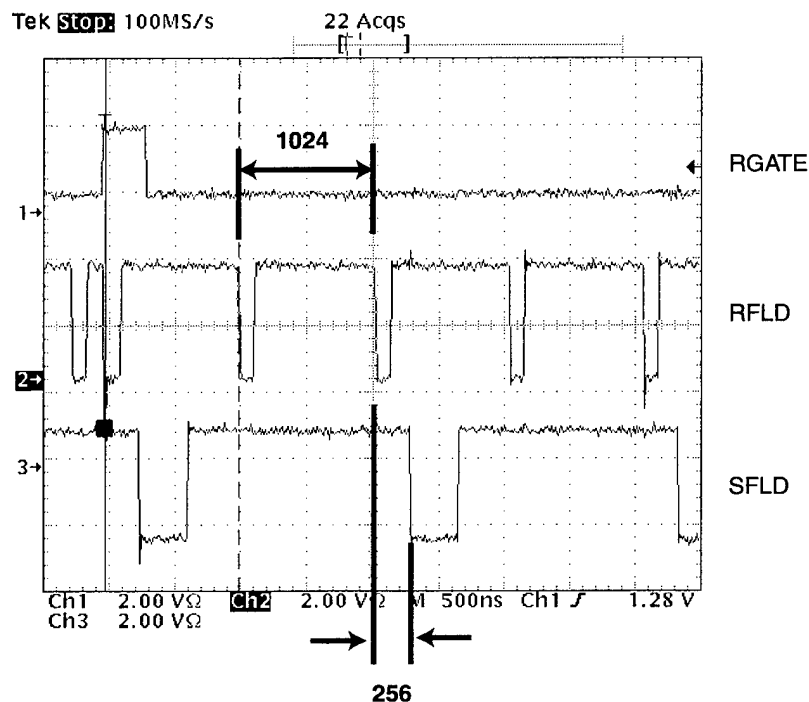


Figure 6-4. Waveforms recorded on an oscilloscope with the chip operating at its full design frequency. The upper trace shows the input RGATE signal that starts the processing of a new coherent processing interval. The middle trace shows the waveform on the RFLD diagnostic output. Each negative pulse shows when reference data about the signal transmitted by the radar are recorded on the chip. The time between pulses is the programmed "pulse repetition interval" for the radar. The bottom trace shows the waveform on the SFLD diagnostic output. Each negative pulse shows when data about the signal received by the radar are stored in one of the two memory banks on the chip. These pulses are delayed from their corresponding RFLD pulses by the programmed target range delay, adjusted for range walk.

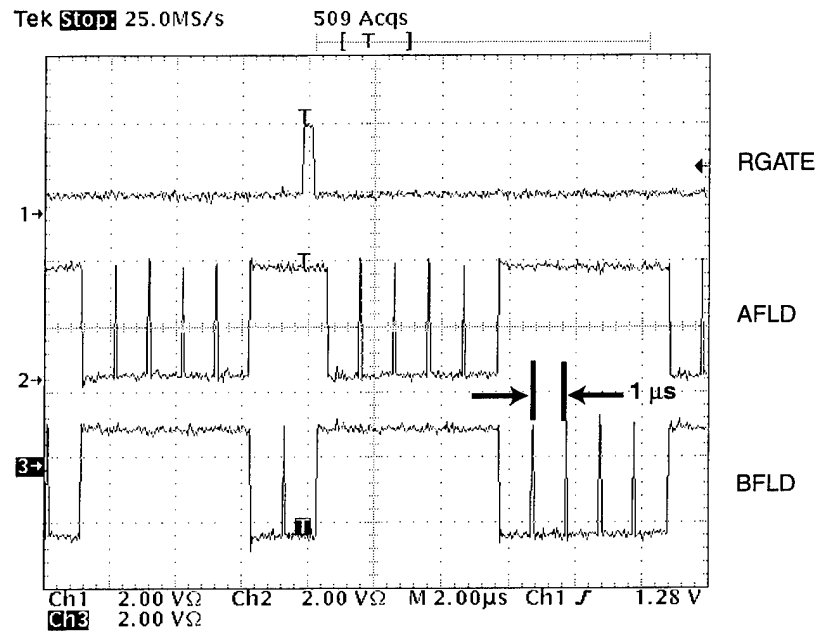


Figure 6-5. Additional waveforms recorded with the chip operating at its full design frequency. The upper trace again shows the input RGATE. The lower two traces show the waveforms on the diagnostic outputs AFLD and BFLD, where negative pulses indicate when correlation data are being stored into each of the two banks of "presum" memory. The chip has been programmed to perform a presum of five pulses.



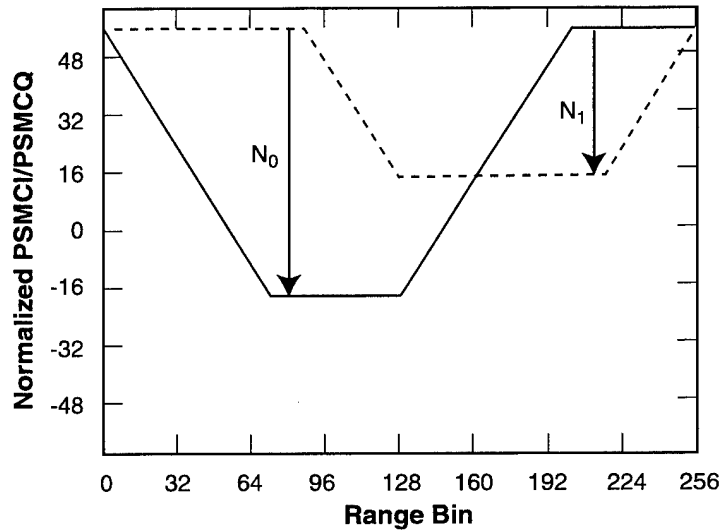


Figure 6-6. Processed correlation data read from the chip with the radar clock at 800 MHz. The solid curve is the in-phase component PSMCI; the dotted curve is the quadrature component PSMCQ. Both signals have been scaled to take out factors arising from the cosine/sine weighting and the presum value. The signal in-phase input SI was a square wave with 128 0's and 128 1's. The reference in-phase input RI was a section from that square wave comprising 72 0's followed by 40 1's. The quadrature inputs were both 0. The observed output is exactly what theory predicts: linear ramps between baselines at half the code length ( $112/2 = 56$  in this case) and values reduced from that by the number of 0's (for PSMCI) and 1's (for PSMCQ) in the reference pattern.

## 7. ADVANCED SILICON TECHNOLOGY

### 7.1 TOTAL DOSE RADIATION EFFECTS ON HARDENED BURIED-OXIDE FDSOI NMOS

Fully depleted silicon-on-insulator (FDSOI) technology is of interest for radiation hard applications because of the dielectric isolation and limited charge collection volume provided by the buried-oxide (BOX) layer. SOI circuits have been shown to be less prone to single-event-upset damage than bulk CMOS technologies [1]. FDSOI is also advantageous for high-performance, low-power, low-voltage applications. However, total dose radiation hardening is challenging in FDSOI because radiation-induced positive charge trapping in the BOX causes NMOS degradation, i.e., a reduction in threshold voltage and an increase in leakage current [2]. In advanced SOI processes with thin gate oxides (<8 nm) and with mesa isolated transistors, most or all charge trapping occurs in the BOX layer. The radiation damage has a greater effect on NMOS than PMOS performance because positive charge trapping in the BOX induces a negative threshold shift for NMOS, i.e., more leakage current, and a positive threshold shift for PMOS, i.e., less leakage current.

The Defense Threat Reduction Agency and Naval Research Laboratory (DTRA/NRL) have developed a technique to harden SOI wafers via implanting selected species in the BOX close to the SOI/BOX interface [3],[4]. Ibis Technology Corporation, a United States SOI wafer vendor, implemented the SOI hardening process on Advantox150™ wafers, which are the latest generation of low-dose SIMOX wafers [5]. For the radhard wafers studied in this work, silicon was the implanted species.

Transistors were fabricated at the Lincoln Laboratory Microelectronics Laboratory class 10 clean room using our unhardened, 0.25- $\mu\text{m}$  FDSOI CMOS process [6]. The mesa isolation process was slightly modified to suppress parasitic sidewall conduction on the mesa transistors (edge effect). FDSOI NMOS transistors were fabricated on conventional (control) and hardened (radhard) wafers. NMOS transistors were then characterized before and after X-ray irradiation up to a total dose of 1 Mrad ( $\text{SiO}_2$ ).

The Lincoln Laboratory 0.25- $\mu\text{m}$  FDSOI process features mesa-isolated SOI islands thinned to 50-nm final thickness, a 7.3-nm gate oxide, 0.25- $\mu\text{m}$ -drawn dual-doped polysilicon gates, low-pressure tetraethoxysilane (LPTEOS) oxide spacers, and self-aligned silicided source, drain, and poly gates, as shown in Figure 7-1. The backend process has three metal levels with aluminum damascene stacked contact and via plugs with chemical-mechanical planarization (CMP) steps at contact, via, and intermetal dielectric layers. The process was designed for an operating voltage  $V_{DD}$  of 2 V with a low drain bias threshold voltage of roughly  $V_{DD}/4$ .

No specific issue such as particle contamination, surface roughness, defects, bow, or warp was identified during the fabrication process, and all in-line process monitors yielded similar results for the control and radhard wafers. The mean BOX thickness was between 152 and 154 nm for both wafer types with a standard deviation lower than 0.5%. Upon process completion, over 300 transistor measurements

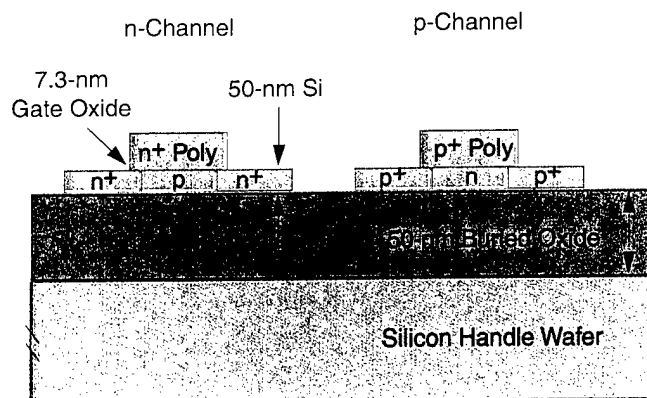


Figure 7-1. Schematic diagram describing MIT Lincoln Laboratory's 0.25- $\mu\text{m}$  fully depleted silicon-on-insulator (FDSOI) CMOS process.

and 500 test structures were characterized. In general, NMOS transistors fabricated on control and radhard wafers yielded similar electrical characteristics ( $<10\%$  difference). The minimal difference in the low-drain-bias threshold voltage, subthreshold slope, and back-channel threshold voltage observed between the two types of wafers is a preliminary indication that the BOX radiation hardening process did not affect the pre-radiation electrical characteristics of the NMOS. Results reported below are for  $W = 4.8 \mu\text{m}$ ,  $L = 0.5 \mu\text{m}$  NMOS annular gate transistors, i.e., edgeless, circular-shaped gate. Non-minimum gate length devices were studied first to separate contribution from short-channel effects.

Radiation testing was conducted using a 10-keV X-ray tube of an Aracor 4100. Transistors were biased in the on-gate condition during irradiation where the gate is biased at 2 V, all other terminals grounded. NMOS received incremental X-ray doses totaling 10, 30, 100, 300, 600, and 1000 krad ( $\text{SiO}_2$ ). Current-voltage curves were taken for pre- and post-radiation increments to characterize front-channel and back-channel threshold voltages and overall radiation effects. At low drain bias ( $V_D = 50 \text{ mV}$ ), the front- and back-channel threshold voltages were calculated by extrapolation from the maximum transconductance point. At high drain bias ( $V_D = 2 \text{ V}$ ), threshold voltages were defined as the gate bias  $V_G$  at a given drain current  $I_D$ , as specified in the next section.

Figures 7-2(a) and 7-2(b) are the front-channel  $I_D V_G$  at a drain bias  $V_D$  of 50 mV (wafer at 0 V) for the control and radhard wafers, respectively. As the cumulative X-ray dose increases, the  $I_D V_G$  curves shift toward the left, indicating a decrease in the threshold voltage and an increase in the leakage current at  $V_G = 0 \text{ V}$ . It is apparent in these figures that the NMOS transistors have very similar pre-radiation characteristics,

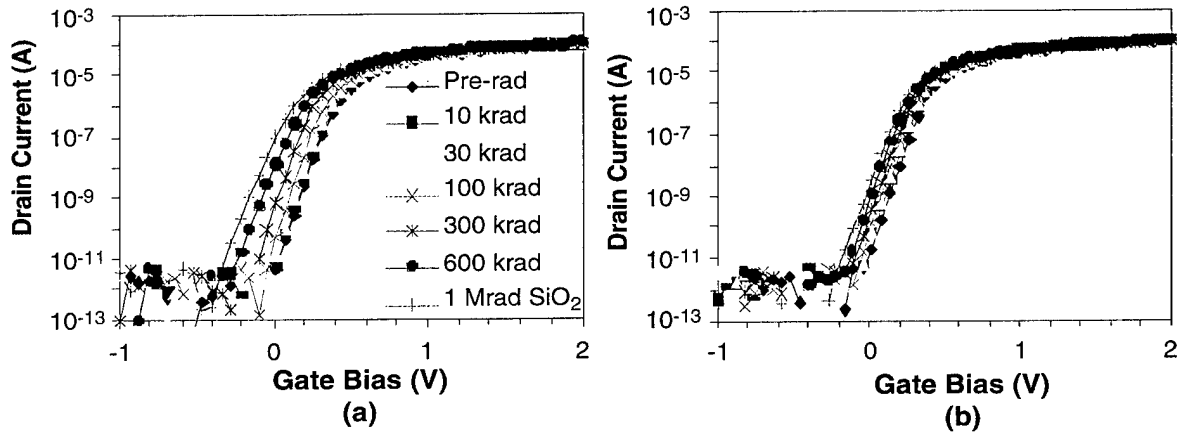


Figure 7-2. Front-channel  $I_D V_G$  at  $V_D = 50$  mV (wafer bias 0 V) for  $W = 4.8$   $\mu\text{m}$ ,  $L = 0.5$   $\mu\text{m}$  NMOS on (a) control Advantox150™ and (b) radhard Advantox150™ substrates for total X-ray radiation dose up to 1 Mrad ( $\text{SiO}_2$ ).

but upon radiation appear to degrade less rapidly on the radhard wafer than on the control wafer. In Figure 7-3(a), the extrapolated front-channel threshold voltage  $V_{t,low}$  shift is plotted vs the total radiation dose for both the control and radhard wafers. Note that the negative shift in  $V_{t,low}$  with increasing radiation dose is consistent with positive charge buildup in the BOX.

Up to 30 krad, the shift in  $V_{t,low}$  is nominally the same (approximately  $-30$  mV) for both wafer types. From 300 krad up to 1 Mrad,  $V_{t,low}$  shift is roughly two times higher for the NMOS on control wafer ( $-240$  mV) than for the NMOS on radhard substrate ( $-140$  mV). As shown in Figure 7-3(b), the subthreshold swing  $S$  is 67 mV/dec before radiation for transistors on both wafer types. Starting at 300 krad ( $\text{SiO}_2$ ),  $S$  degrades more rapidly for the control wafer. At 1 Mrad ( $\text{SiO}_2$ ),  $S$  is roughly 90 mV/dec for the NMOS on the control wafer and only 75 mV/dec for NMOS on the radhard wafer. The change in  $V_{t,low}$  and subthreshold swing indicate a faster degradation of the NMOS on the control wafer than on the radhard wafer, consistent with the buildup of positive charges and traps in the BOX.

The  $I_D V_G$  curve at  $V_D = 50$  mV is reported in Figure 7-4 for the same device as shown in Figure 7-2(b), with the back channel in accumulation ( $-30$  V applied to the wafer). This measurement shields the channel from charges in the BOX or at the SOI/BOX interface, so that any shift observed can only be caused by the front gate oxide and interface since our SOI islands are mesa isolated. The extrapolated threshold voltage shift  $V_{t,A50}$ , extracted like  $V_{t,low}$ , is small ( $< -50$  mV) up to 1 Mrad, which indicates negligible radiation effects on the front-channel oxide and interface. This is consistent with a thin gate oxide, which is 7 nm in our process. A similar characteristic was observed for NMOS on the control substrate. We conclude that in our FDSOI NMOS, charge trapping occurs in total in the BOX.

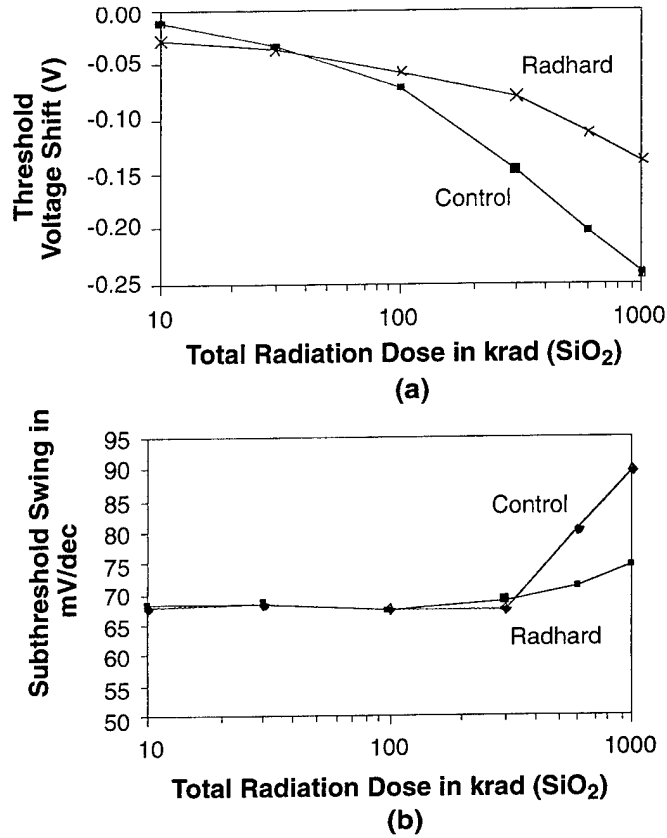


Figure 7-3. (a) Front-channel threshold shift  $V_{t,low}$  at  $V_D = 50$  mV and (b) subthreshold voltage swing vs total radiation dose for  $W = 4.8$   $\mu\text{m}$ ,  $L = 0.5$   $\mu\text{m}$  NMOS fabricated on control and radhard Advantox150™ wafers.

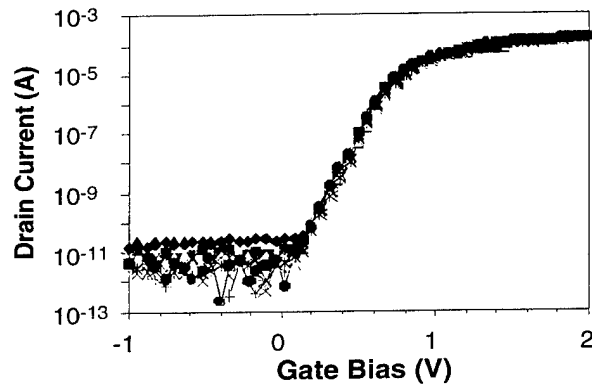


Figure 7-4. Front-channel  $I_D V_G$  at  $V_D = 50$  mV with back gate accumulated (wafer bias  $-30$  V) for  $W = 4.8$   $\mu\text{m}$ ,  $L = 0.5$   $\mu\text{m}$  NMOS on radhard Advantox150™ substrates for total X-ray radiation dose up to 1 Mrad (SiO<sub>2</sub>).

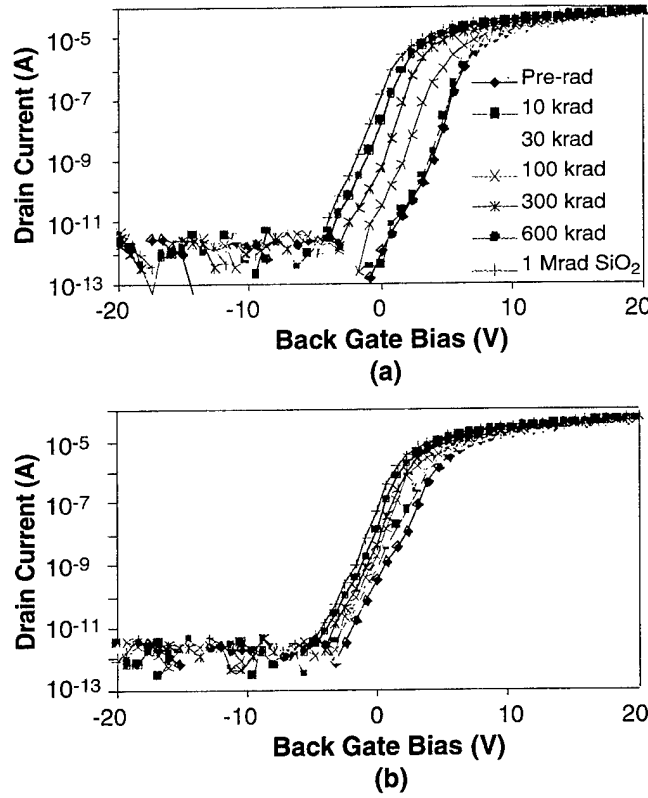


Figure 7-5. Back-channel  $I_D V_W$  at  $V_D = 50$  mV (gate bias 0 V) for  $W = 4.8$   $\mu\text{m}$ ,  $L = 0.5$   $\mu\text{m}$  NMOS on (a) control Advantox150<sup>TM</sup> and (b) radhard Advantox150<sup>TM</sup> wafers for total X-ray radiation dose up to 1 Mrad ( $\text{SiO}_2$ ).

Shown in Figures 7-5(a) and 7-5(b) are the back-channel  $I_D V_W$  for NMOS on the control and radhard wafers, respectively. The back-channel threshold voltage, defined as the gate voltage for a drain current  $I_D$  of  $20 \text{ nA} \times W/L$ , degrades faster for NMOS on the control wafer than NMOS on the radhard wafer. The threshold shift at 1 Mrad ( $\text{SiO}_2$ ) is 5.6 V for the control wafer vs 3.5 V for the radhard wafer. This result confirms that the BOX of the radhard wafer is less sensitive to radiation damage than the BOX of the control, conventional SOI wafer. The Si implanted in the BOX of the radhard wafer is effective in reducing the effect of positive charge trapping in the BOX.

The radiation hardness advantage achieved with the BOX hardening process is shown more markedly on the  $I_D V_G$  curves at  $V_D = 2$  V in Figures 7-6(a) and 7-6(b) for NMOS on control and radhard wafers, respectively. Very small shift in the  $I_D V_G$  curves is observed for the radhard wafer. As shown in Figure 7-7(a), the threshold voltage  $V_{t,high}$ , defined as the gate voltage for a drain current of  $0.1 \mu\text{A} \times W/L$ , shifts by 10–20 mV for both wafers up to 100 krad. The shift is still very small compared to the nominal

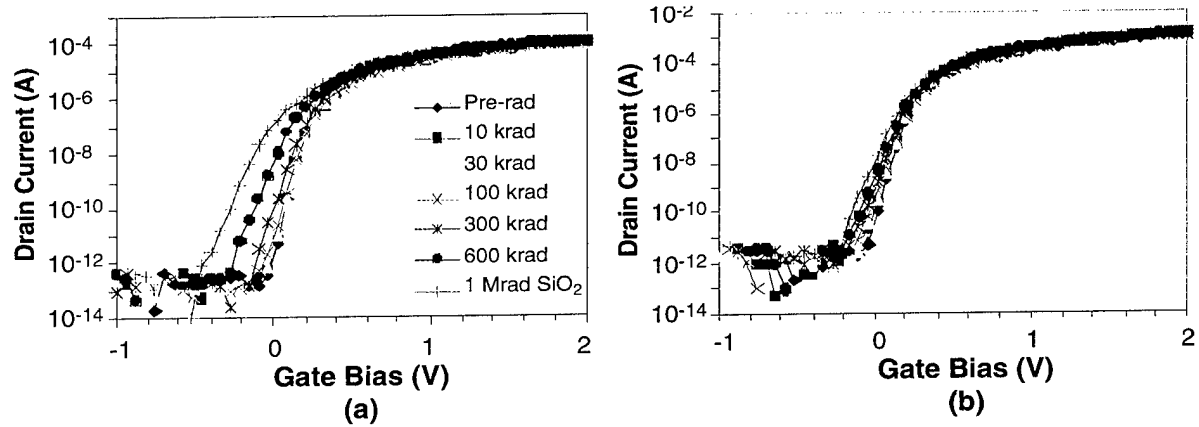


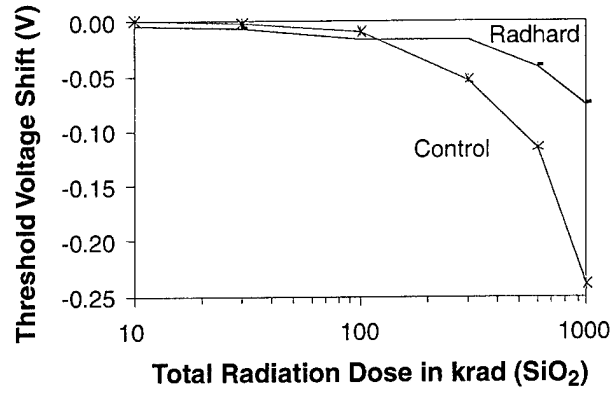
Figure 7-6. Front-channel  $I_D V_G$  at  $V_D = 2$  V (wafer bias 0 V) for  $W = 4.8 \mu\text{m}$ ,  $L = 0.5 \mu\text{m}$  NMOS on (a) control and (b) radhard Advantox150™ substrates for total X-ray radiation dose up to 1 Mrad ( $\text{SiO}_2$ ).

pre-radiation threshold voltage. At 1 Mrad ( $\text{SiO}_2$ ),  $V_{t,high}$  shift is larger for the NMOS on the control wafer ( $-240$  mV) than for the NMOS on the radhard wafer ( $-75$  mV). Consequently, as shown in Figure 7-7(b), the off-state leakage current, defined as  $I_D$  at  $V_D = 2$  V and  $V_G = 0$  V, is 2000 nA on the control wafer vs 10 nA on the radhard wafer.

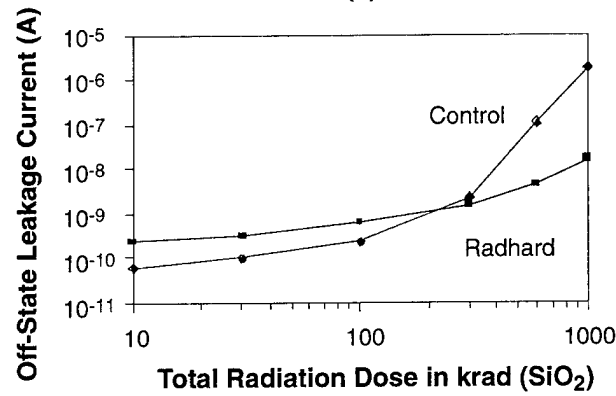
Our results show that the DTRA/NRL BOX hardening process implemented in Advantox150™ SIMOX wafers greatly increases total dose hardness of Lincoln Laboratory FDSOI NMOS transistors up to a total X-ray dose of 1 Mrad ( $\text{SiO}_2$ ) with a significant reduction in threshold voltage shift (3 times) and off-state leakage current (200 times) compared to the NMOS fabricated on the conventional SIMOX wafers. These results are, to our knowledge, the smallest X-ray irradiation damage reported to date on FDSOI NMOS transistors. Further testing is ongoing to characterize radiation effects as a function of the NMOS layout (mesa vs annular, i.e., edge vs edgeless devices), the NMOS bias during irradiation, the channel length (down to  $0.25 \mu\text{m}$ ), and the BOX radiation hardening process. Impact on PMOS performance will also be assessed.

P. Gouker	E. Austin
P. Wyatt	J. Burns
C. Keast	W. Jenkins*
H. Hughes*	

\*Author not at Lincoln Laboratory.



(a)



(b)

Figure 7-7. (a) Front-channel threshold shift  $V_{t,high}$  at  $V_D = 2$  V and (b) off-state leakage current  $I_D$  at  $V_G = 0$  V and  $V_D = 2$  V vs total radiation dose for  $W = 4.8$   $\mu\text{m}$ ,  $L = 0.5$   $\mu\text{m}$  NMOS fabricated on control radhard Advantox150<sup>TM</sup> wafers.



## REFERENCES

1. A. J. Auberton-Herve, *International Electron Devices Meeting Technical Digest* (IEEE, Piscataway, N.J., 1996).
2. J. R. Schwank, M. R. Shaneyfelt, P. E. Dodd, J. A. Burns, C. L. Keast, and P. W. Wyatt, *IEEE Trans. Nucl. Sci.* **47**, 604 (2000).
3. H. Hughes and P. McMarr, U.S. Patent No. 5,795,813.
4. P. J. McMarr, R. K. Lawrence, H. L. Hughes, W. C. Jenkins, B. J. Mrstik, G. G. Jernigan, and M. E. Twigg, presented at the 1999 HEART Conference.
5. R. Dolan, M. Alles, M. Anc, B. Cordts, J. Dunne, M. Gindlseperger, B. Hornblowe, T. Y. Jang, M. Powell, J. Blake and T. Nakai., *Proceedings of the 2000 IEEE International SOI Conference* (IEEE, Piscataway, N.J., 2000).
6. H. I. Liu, J. A. Burns, C. L. Keast, and P. W. Wyatt, *IEEE Trans. Electron Devices* **45**, 1099 (1998).

